Remote Sensing of Environment 141 (2014) 168–187

Contents lists available at ScienceDirect

Remote Sensing of Environment

journal homepage: www.elsevier.com/locate/rse

An Anisotropic Flat Index (AFX) to derive BRDF archetypes from MODIS

Ziti Jiao [a,b,*], Michael J. Hill [c,**], Crystal B. Schaaf [d,***], Hu Zhang [a,b], Zhuosen Wang [d], Xiaowen Li [a,b]

[a] State Key Laboratory of Remote Sensing Science, and School of Geography, Beijing Normal University, Beijing 100875, China
[b] Beijing Key Laboratory of Environmental Remote Sensing and Digital City, Beijing Normal University, Beijing 100875, China
[c] Department of Earth System Science and Policy, University of North Dakota, Clifford Hall, 4149 University Avenue, Grand Forks, ND 58202, USA
[d] School for the Environment, University of Massachusetts Boston, 100 Morrissey Blvd., Boston, MA 02125, USA

ARTICLE INFO

Article history:
Received 22 February 2013
Received in revised form 22 October 2013
Accepted 26 October 2013
Available online 26 November 2013

Keywords:
BRDF
MODIS
Vegetation index
Anisotropic Flat Index (AFX)
BRDF typology
BRDF archetypes
Vegetation structure
Multiangle remote sensing
Linear model
EOS land validation core sites
A priori knowledge

ABSTRACT

Spectral vegetation indices can be generalized as a function of surface reflectance with respect to wavelength. However, there is significant information on vegetation structure embedded in the anisotropic effects of the target. In this study, we describe and characterize a new vegetation index, the Anisotropic Flat Index (AFX) that captures this anisotropic scattering information and can be derived from the Moderate Resolution Imaging Spectroradiometer (MODIS) bidirectional reflectance distribution function (BRDF) product suite (MOD43A1). The AFX is created by normalization of net scattering magnitude (obtained from volumetric and geometric-optical scattering) with the isotropic scattering. The AFX summarizes the variability of basic dome-bowl anisotropic reflectance patterns of the terrestrial surface. A classification scheme for BRDF typology is created based on AFX archetypes that capture characteristic BRDF shape types. This study fully characterizes AFX in a number of steps. First, sensitivity to random noise and observation geometries is explored by comparing the AFX with other variables derived from field measurements that comprehensively sample the viewing hemisphere. Second, AFX is compared with normalized difference vegetation index (NDVI) values using field measurements from many ground campaigns, as well as global MODIS observations from EOS Land Validation Core Sites (LVCS). Third, a BRDF typology is developed by classification of an a priori database of BRDF archetypes from field measurements, and from MODIS observations that cover the full range of vegetation types from grasslands to closed forest (MCD43A). Fourth, the response of AFX to the parameter variability of canopy architectures and background optical properties for three vegetation types with discontinuous woody canopies is investigated through the use of a 5-Scale BRDF model simulation. Finally, global BRDF archetypes are mapped and discussed through the use of a global high-quality MODIS BRDF/albedo gap filled product (MCD43GF). The results show that the AFX summarizes BRDF archetypes and provides additional information on vegetation structure and other anisotropic reflectance characteristics of the land surface.

1. Introduction

Methods that collapse spectral and (or) directional scattering data from remote sensing into simplified index formulations are widely accepted for retrieval of land surface information. Such vegetation indices have proven valuable in many fields of terrestrial science applications that aim to monitor and characterize the Earth's vegetation cover. Conventional spectral vegetation indices can be derived from surface reflectance using specific wavelengths (Huete, 1988; Myneni, Hall, Sellers, & Marshak, 1995), and have been widely used as indirect measures of various biophysical and biochemical variables, including leaf area index (LAI) (Boegh et al., 2002; Chen & Cihlar, 1996; Haboudane, Miller, Pattey, Zarco-Tejada, & Strachan, 2004), the fraction of photosynthetically active radiation absorbed by vegetation (FPAR) (Cohen, Maiersperger, Gower, & Turner, 2003; Di Bella, Paruelo, Becerra, Bacour, & Baret, 2004; Myneni, Ramakrishna, Nemani, & Running, 1997) and vegetation water content (Ceccato, Tarantola, Jacquemoud, Gregoire, & Flasse, 2001; Tucker, 1980). With conventional spectral vegetation indices, the anisotropic effects of the target are usually treated as perturbing factors considered to be a source of uncertainty in quantitative assessment. Therefore, many methods for deriving traditional spectral vegetation indices usually utilize remote sensing observations near or normalized to nadir, and the angular variations of the radiometric signal are frequently removed through an angular normalization technique (Leroy & Roujean, 1994; Lucht, Schaaf, & Strahler, 2000). Global land cover maps have been developed mainly by using multispectral nadir signals and the change in those multispectral signals through an annual cycle, including data from sensors such as the Advanced Very High Resolution Radiometer (AVHRR, Loveland et al., 2000), MODIS (Friedl et al., 2002, 2010), SPOT-Vegetation (Bartrlev, Belward, Erchov, & Lsaev, 2003) and the Medium Resolution Imaging Spectrometer (MERIS, Bicheron et al., 2008). On the other

* Correspondence to: Z. Jiao, State Key Laboratory of Remote Sensing Science, and School of Geography, Beijing Normal University, Beijing 100875, China.
** Corresponding author.
*** Corresponding author.
E-mail addresses: jiaozt@bnu.edu.cn (Z. Jiao), hillmj@aero.und.edu (M.J. Hill), crystal.schaaf@umb.edu (C.B. Schaaf).

0034-4257/$ – see front matter © 2013 Elsevier Inc. All rights reserved.
http://dx.doi.org/10.1016/j.rse.2013.10.017

hand, both measurement and modeling have shown that multi-angular remote sensing can enhance the retrieval of global land surface properties, including albedo (Bicheron & Leroy, 2000; Martonchik, Pinty, & Verstraete, 2002; Schaaf et al., 2002), land covers (DE Colstoun & Walthall, 2006; Galvao, Roberts, Formaggio, Numata, & Breunig, 2009; Heiskanen & Kivinen, 2008; Jiao & Li, 2012; Jiao et al., 2011) and other key surface biophysical quantities for ecological and biological studies (Asner, 2000; Chen, Liu, Leblanc, Lacaze, & Roujean, 2003; Chopping et al., 2008; Gao, Schaaf, Strahler, Jin, & Li, 2003; Wang et al., 2011).

The anisotropic effects of the land surface on spectral reflectance can be captured by angular vegetation indices (thus BRDF shape indicators). Angular vegetation indices have been derived from the model parameters of kernel-driven linear BRDF models (Gao et al., 2003; Roujean & Lacaze, 2002). An anisotropic factor (ANIF), an anisotropic index (ANIX) and the normalized difference between red and near infrared (NIR) ANIX (NDAX) (Sandmeier & Deering, 1999; Sandmeier, Muller, Hosgood, & Andreoli, 1998) have all been suggested as ways to explore the physical mechanism of hyper-spectral BRDF effects and their relationship to land cover types. The hot-dark spot index (HDS) and the normalized difference between hotspot and dark spot (NDHD) (Chen, Menges, & Leblanc, 2005; Chen et al., 2003; Lacaze et al., 2002; Leblanc et al., 2005) are sensitive to the angular reflectance of photosynthetically active radiation (PAR) from sunlit and shaded leaves, and have been used to derive measures of foliage clumping. Roujean and Lacaze (2002) used model parameters derived from satellite retrievals with a kernel-driven linear BRDF model for global mapping of vegetation parameters. Gao et al. (2003) used similar model parameters and suggested a Structural Scattering Index (SSI). The HDS has also been used in combination with the NDVI to generate the normalized hotspot-signature vegetation index (NHVI) for the estimation of leaf area index (Hasegawa, Matsuyama, Tsuzuki, & Sweda, 2010).

These angular vegetation indices have been applied in various studies that seek to retrieve additional information to enhance assessment of land cover/dynamics (D'Entremont, Schaaf, Lucht, & Strahler, 1999; Gao et al., 2003; Jiao et al., 2011; Roujean & Lacaze, 2002; Sandmeier & Deering, 1999; Su, Chopping, Rango, Martonchik, & Peters, 2007) and canopy structures (e.g., canopy density, foliage clumping factor) (Chen et al., 2003, 2005; Gao et al., 2003; Hill, Averill, Jiao, Schaaf, & Armston, 2008, Hill et al., 2011; Lacaze, Chen, Roujean, & Leblanc, 2002; Leblanc & Chen, 2001, Leblanc et al., 2005; Nolin, 2004). However, to date, angular indices have not been used to derive a standard classification of BRDF typology, i.e., to generalize BRDF archetypes from various realistic BRDF shapes into a few BRDF-based classes for potential ecological applications and thus building on the early work of Strugnell and Lucht (2001) and Strugnell, Lucht, and Schaaf (2001).

The early efforts by Strugnell and Lucht (2001) and Strugnell et al. (2001) used 68 field multi-angle measurements (all measurements have been utilized in this study as well) to derive 25 so-called BRDF-based classes by cross walking with ecological land cover types. A major challenge for this method results from more complex heterogeneous environments within a surface type that tend to generate a high within-class BRDF variation (e.g., areas with heterogeneous patchiness resulting from forest fires or deforestation, and areas with a wide range of discontinuous tree canopy cover fractions and spatial arrangements). With 13 years of MODIS BRDF model parameter data accumulated, various efforts have been made to apply these model parameter data to estimates of biophysical parameters (e.g., Landsat albedo by Shuai, Masek, Gao, & Schaaf, 2011). A major challenge in directly using the entire per-pixel MODIS BRDF parameter data results in conjunction with data from other sensors is the pixel scale mismatch between different spatial resolution images. Román et al. (2013) pointed out that spatial scale errors can produce relatively high retrieval uncertainties in validating albedo measurements acquired from space. At present, cross walking a land cover map with BRDF shapes remains a desired approach despite its attendant classification accuracy and generalization issues. Therefore, developing a framework to extract the basic BRDF shapes from the multiyear MODIS model parameter data remains an important challenge. It is particularly important to determine the sensitivity of these basic BRDF shapes to canopy architecture associations and background optical properties, especially for discontinuous multilayer vegetation canopies. Additionally, these basic BRDF shapes could be used as a priori knowledge in estimation of biophysical parameters for certain ecological applications.

This study provides a major advance on the work of Strugnell and Lucht (2001) and Strugnell et al. (2001) by combining MODIS BRDF model parameter data into a more generic Anisotropic Flat Index (AFX) based on kernel-driven linear BRDF model theory. The work by Strugnell et al. (2001) was a quite rudimentary attempt to develop an a priori BRDF database, and is actually no longer used by the MODIS algorithm which has access to considerable NASA processing power and the luxury of using the most recent BRDF retrieval for that pixel directly. But for applications which do not have access to such resource, a generalized anisotropy flat index provides some ancillary information. The study a) explores the general characteristics of AFX in relation to the anisotropic reflectance patterns of land surface; b) investigates the uncertainty and sensitivity of AFX to observation geometries and random noise; c) analyzes the new information provided by the AFX in comparison with a traditional spectral vegetation index for MODIS observations and explores its response to canopy architectures and background optical properties for three vegetation types with discontinuous woody canopies through use of a 5-Scale BRDF model simulation; d) generates an a priori database of BRDF archetypes based on AFX; and e) maps BRDF archetypes for the globe and initially compares these to MODIS International Geosphere-Biosphere Program (IGBP) land cover classes.

2. Methods

2.1. Theoretical basis

2.1.1. Ross–Li model

The Ross–Li model is a further development of kernel-driven Roujean BRDF model (Roujean, Leroy, & Deschamps, 1992) that is linear combination of three basic scattering components: isotropic scattering, volume scattering and geometric-optical surface scattering. This model adopted a general form (Lucht et al., 2000; Roujean et al., 1992; Wanner, Li, & Strahler, 1995):

$$R(\theta_v,\theta_s,\Delta\phi\lambda) = f_{\mathrm{iso}}(\lambda) + f_{vol}(\lambda)K_{\mathrm{vol}}(\theta_v,\theta_s,\Delta\phi) + f_{\mathrm{geo}}(\lambda)K_{\mathrm{geo}}(\theta_v,\theta_s,\Delta\phi) \quad (1)$$

where $f_{\mathrm{iso}}(\lambda)$, $f_{vol}(\lambda)$ and $f_{\mathrm{geo}}(\lambda)$ are the spectrally dependent model parameters. $K_{\mathrm{vol}}(\theta_v,\theta_s,\Delta\phi)$ and $K_{\mathrm{geo}}(\theta_v,\theta_s,\Delta\phi)$ are kernel functions of view zenith θ_v, illumination zenith θ_s and relative azimuth $\Delta\phi$, providing shapes for volumetric scattering and geometric-optical scattering BRDFs; $f_{\mathrm{iso}}(\lambda)$ is a spectral constant for isotropic scattering that determines optical properties in relation to reflectance and transmittance of vegetation foliage and background; $f_{vol}(\lambda)$ and $f_{\mathrm{geo}}(\lambda)$ are spectral constants that weight the two BRDFs; $R(\theta_v,\theta_s,\Delta\phi\lambda)$ is bidirectional reflectance distribution function in waveband λ.

The Ross–Li model was originally designed to include a series of kernels for various land cover types in MODIS (Wanner et al., 1995). Volumetric scattering kernels include RossThick kernel for a big leaf area index (LAI ≫ 1) and RossThin kernel for a small LAI (LAI ≪ 1), which were originally developed by (Roujean et al., 1992), based on an assumption of a single-scattering approximation of the radiative transfer (RT) theory by Ross (1981). These two volumetric kernels take the reciprocal form, i.e., the sunlit component is simply assumed to vary as reciprocal of cosine of view zenith (Roujean et al., 1992; Wanner et al., 1995). Geometric-optical kernels include the LiSparse, the LiDense (Wanner et al., 1995) kernels for discrete clumping vegetation crown with low and high density, and the LiTransit (Gao, Li, Strahler, & Schaaf, 2000; Li, Gao, Chen, & Strahler, 1999) kernel for

vegetation crowns with densities varying from sparse to dense at a given threshold of viewing and solar geometry. These geometric-optical kernels can also take a reciprocal form by empirically adding a cosine of the sunlit component (Gao et al., 2000; Li et al., 1999; Lucht et al., 2000; Roujean et al., 1992; Wanner et al., 1995). The current operational MODIS BRDF algorithm has adopted the RossThick–LiSparse Reciprocal (RTLSR) model for the routine MODIS BRDF/Albedo product. This model has also been adopted for the VIIRS (Visible/Infrared Imager/Radiometer Suite) Albedo and Bidirectional Reflectance Climate Data Records on board the platforms of the Suomi National Polar-orbiting Partnership (NPP) for dark surfaces (e.g., vegetation).

2.1.2. Relationship of AFX to model parameters

Given the pre-determined structure parameters in the kernel function, these kernels are just trigonometric functions regarding viewing and solar geometries and the relative azimuthal angles between them; therefore, they can be pre-calculated for given viewing and solar geometry or directional–hemispherical integral or bi-hemisphere integral. An integral of the viewing hemisphere for these kernels results in directional–hemispherical integral value, followed by further integration of the solar hemisphere to generate a bi-hemispherical integral value, usually marked as H_{ker} (Lucht et al., 2000). Therefore, for a given kernel, H_{ker} is a constant value in relation to a certain scattering type.

For a given pixel, if sufficient multiangular observations have been accumulated to adequately sample the viewing hemisphere, Eq. (1) can be inverted for three model parameters as spectral constants, and then integration over the both viewing and illumination hemisphere can be accomplished to acquire the bi-hemispherical reflectance, i.e., white sky albedo (WSA) in MODIS BRDF/Albedo product (Lucht et al., 2000; Schaaf et al., 2002)

$$WSA(\lambda) = f_{\mathrm{iso}}(\lambda) + f_{\mathrm{vol}}(\lambda)H_{\mathrm{ker\_vol}} + f_{\mathrm{geo}}(\lambda)H_{\mathrm{ker\_geo}}. \quad (2)$$

By simply normalizing Eq. (2) on both sides by the isotropic parameter to remove the spectral reflectance amplitude, the new angular index AFX can be generated with Eq. (3)

$$\frac{WSA(\lambda)}{f_{\mathrm{iso}}(\lambda)} = \mathrm{AFX} = 1 + \frac{f_{\mathrm{vol}}(\lambda)}{f_{\mathrm{iso}}(\lambda)} \times H_{\mathrm{ker\_vol}} + \frac{f_{\mathrm{geo}}(\lambda)}{f_{\mathrm{iso}}(\lambda)} \times H_{\mathrm{ker\_geo}}. \quad (3)$$

Again, $H_{\mathrm{ker\_vol}}$ and $H_{\mathrm{ker\_geo}}$ are the predetermined bi-hemispherical integral values for the volumetric and geometric-optical kernels. For the RTLSR model, $H_{\mathrm{RossThick}} = 0.189184$ and $H_{\mathrm{LiSparseR}} = -1.377622$. The parameters, $f_{\mathrm{geo}}(\lambda)$ and $f_{\mathrm{vol}}(\lambda)$ are the two spectral constants that weight BRDF shapes, while $f_{\mathrm{iso}}(\lambda)$ is a spectral constant for isotropic scattering that determines the spectral reflectance amplitude. Here, we define $\mathrm{WSA}(\lambda)/f_{\mathrm{iso}}(\lambda)$ as the new Anisotropic Flat Index (AFX) to reflect these BRDF effects. Therefore, Eq. (3) combines the model parameters with the bi-hemispherical kernel integral values into a more general index (AFX) that is related to the variability of the BRDF shapes of land surfaces.

2.1.3. Relationship of AFX to anisotropic reflectance pattern

It is important to understand the behavior of the estimated AFX under the anisotropic reflectance conditions of different vegetation covers. Since the AFX is derived from a kernel-driven linear BRDF model, a simple review of the general considerations behind the kernel-driven BRDF models is helpful in further understanding the AFX. The kernel-driven BRDF model have followed the central assumption that, for a given heterogeneous land surface, "the surface reflectance may be viewed as a combination of two different component representative of two different bidirectional signatures" (Roujean et al., 1992). One component is the material surface scattering considering the geometrical structure and shadowing effects, and the other is volume scattering represented by randomly located facets which are absorbing and scattering radiation. For discrete tree crowns, a simple understanding of these two components with regard to the within-crown and between-crown scatterings is as predominantly volume and surface scattering components that are respectively modeled with a geometric-optical and radiative-transfer approach that describes randomly-distributed discrete objects comprising a turbid medium (Li, Strahler, & Woodcock, 1995). Although these two scattering components are not necessarily orthogonal, their linear combination has shown a surprising capability to determine the surface anisotropic reflectances of the primary land surfaces with high accuracy (Hu, Lucht, Li, & Strahler, 1997; Lucht & Lewis, 2000; Maignan, Breon, & Lacaze, 2004; Roujean et al., 1992; Schaaf et al., 2002; Wanner et al., 1995). To further examine the characteristics of the AFX, we go back to Eq. (3).

Eq. (3) has same form as Eq. (1) that has been normalized by the isotropic parameter. The bi-hemispherical integral values of Ross kernel series ($H_{\mathrm{ker\_vol}}$) represent positive signs, while bi-hemispherical integral values of Li kernel series ($H_{\mathrm{ker\_geo}}$) represent negative signs. In the operational MODIS BRDF products, negative model parameters are not allowed through the use of a constraining technique, which forces a three-parameter model into a two-parameter model or simply reverts the retrieval to a poorer backup model (Jin et al., 2003; Roman et al., 2011; Schaaf et al., 2002). Such a constraint makes the AFX values vary around unity. Therefore, for normalized volume and surface scattering components, if one component counteracts another, then $\mathrm{AFX} = 1.0$; if the volume scattering component is dominant, then $\mathrm{AFX} > 1.0$; otherwise, $\mathrm{AFX} < 1.0$ indicates that the surface scattering component is dominant.

Furthermore, AFX is related to the variation of the basic dome or bowl BRDF shapes in terms of its values around unity. To explain this, we take the operational RTLSR algorithm for example. Fig. 1 shows 3-D shapes for RossThick and LiSparseR kernels at four given solar zenith angles (15°, 30°, 45° and 60°). The Blue-Green-Red colors indicate the low-to-high transition of kernel values and distinctly reflect the dome-bowl variability of kernel shapes at different illumination geometry. Fig. 1 shows that the volumetric scattering kernels present typical upturned bowl shapes, while the geometric-optical kernels present typical dome shapes. Realistic BRDF shapes are generated by weighting these two kinds of generalized kernel shapes by model parameters, and therefore we can infer that the true BRDF shapes as derived by the RTLSR model would bear resemblance to various dome-bowl shapes. A volume scattering-dominated component ($\mathrm{AFX} > 1.0$) would represent the somewhat more bowl-shaped BRDF curves, while a surface scattering-dominated component ($\mathrm{AFX} < 1.0$) would capture the somewhat more dome-shaped BRDF curves. An $\mathrm{AFX} = 1.0$ would indicate that the volumetric scattering counteracts the geometric-optical scattering and produces a relatively Lambertian surface. This characteristic enables the AFX to support a BRDF-based classification scheme for BRDF typology.

2.2. Assessment of AFX with field measurements

Initially, the AFX is assessed using ground-based measurements that provide accurate land surface information and thus are helpful in understanding the AFX at spatial resolutions of a few meters.

2.2.1. Field BRDF data and processing

Sixty-nine ground measurements were accumulated from different sources (Deering, Eck, & Banerjee, 1999, 1992; Deering, Middleton, & Eck, 1994, Deering et al., 1992; Irons, Campbell, Norman, Graham, & Kovalick, 1992; Kimes, 1983; Kimes et al., 1985; Ranson, Biehl, & Bauer, 1985; Vierling, Deering, & Eck, 1997) and cover a range of land cover types including barren soil with different roughness, sparsely vegetated grass, grass-like or broadleaf crops, and forests. Airborne polarization and directionality of the Earth's reflectances (POLDER, Leroy & Breon, 1996) and cloud absorption radiometer (CAR) data (Tsay, King, Arnold, & Li, 1998) are also included in this collection. Note that CAR/

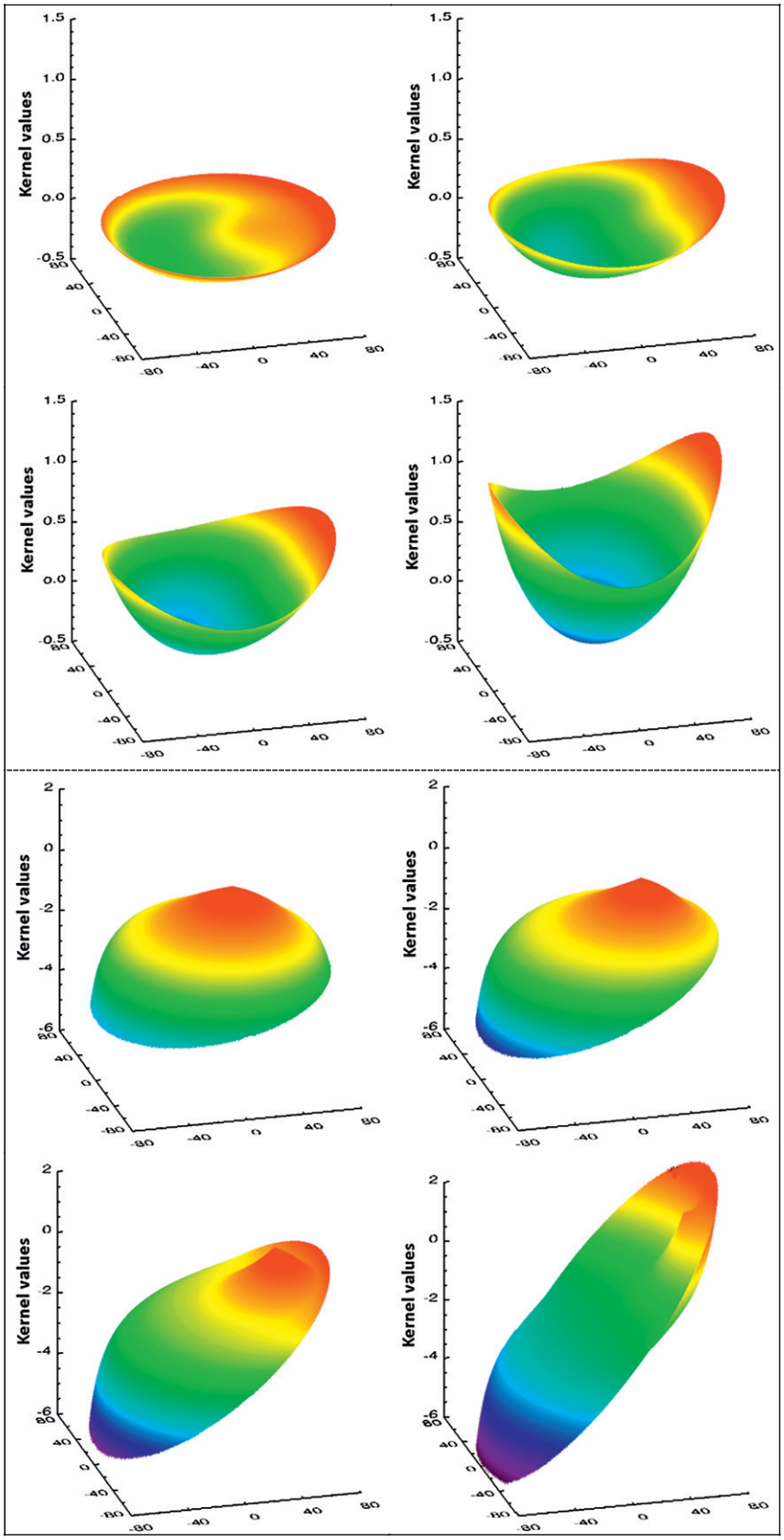

Fig. 1. RossThick (top) and LiSparseR (bottom) kernels with solar zenith angles at 15°, 30°, 45° and 60°.

forest data has a very fine viewing zenith angular resolution (1°) with viewing zenith angles ranging from 0° to 90°, and azimuth angular resolution ranging from 1° to 360°. However, there is only one solar zenith angle position (56.67°) and a strong forward scattering peak occurs from 70° to 90° in the original data, possibly caused by smoke aerosols (Tsay et al., 1998). Because current model kernel combinations do not

characterize the forward scattering peaks well, these data are corrected by removing the measurements beyond 70° of viewing zenith angle. Among these 69 data sets, 27 were previously used for algorithm tests by Hu et al. (1997) and 68 data sets were used to develop 25 BRDF archetypes for a backup algorithm by Strugnell and Lucht (2001) and Strugnell et al. (2001) for the early operational MODIS BRDF and albedo product (the current backup algorithm relies on the most recent high quality retrieval in an updated pixel-by-pixel global BRDF database). Details for every data set are not provided here, and readers are referred to the individual studies cited for more details.

To process the ground measurements, the same inversion strategy that is used for the operational MODIS BRDF/Albedo products is adopted here, resulting in the model inversions that retrieve the parameters of the linear models based on a least-squares method (Lucht et al., 2000). Two internal quality control techniques are used to assess the uncertainty in the model-inversion. The root mean squared error (RMSE) describes the deviation of the RTLSR model-fits from clear observations (Lucht et al., 2000) and is a band-dependent function weighted by the observation quality. Larger RMSE values indicate higher uncertainty in the model fit. The weight of determination (WoD), also designated as the noise amplification factor, describes whether the random noise is amplified or not when the multiangle inputs are processed with the kernel-driven linear models under the conditions of limited and varying angular sampling (Lucht & Lewis, 2000). For simplification, only the WoD of the WSA ($WoD_{\_WSA}$) is calculated in this study.

As mentioned above, a constraining technique is used to limit negative model parameters. This is done by constraining negative parameters to zero while re-fitting a two-parameter model to meet with the least-squares error function by iteration methods. This constraining technique has been adopted in the operational RTLSR algorithm (Jin et al., 2003; Schaaf et al., 2002). With these three quality assurance techniques, the RTLSR model is inverted to obtain model parameters, and then the AFX and other variables including nadir BRDF-adjusted reflectance (NBAR), NDVI and WSA are calculated. The NDVI was calculated with the NBAR at the average solar zenith angle for each data set to limit the angular effects on the target. Examination of the RMSE and $WoD_{\_WSA}$ showed that RMSE had a maximum value of 0.0398 for a desert site (Deering et al., 1992) in red band and a maximum value of 0.0622 for an aspen woodland site (Deering et al., 1992) in NIR band (both <0.1), indicating that all fits by RTLSR algorithm, in general, performed well (Jin et al., 2003; Shuai, Schaaf, Strahler, Liu, & Jiao, 2008). The $WoD_{\_WSA}$ less than 1.0 indicates that the random noise from the observations are suppressed by the RTLSR algorithm for the 69 ground measurements (Lucht & Lewis, 2000).

2.2.2. Analysis of AFX Sensitivity to random noise and observation geometries

The sensitivity of AFX to observation geometry and random noise was compared with three model parameters (f_{geo}, f_{vol} and f_{iso}), white sky albedo (WSA) and the NDVI. First the mean, standard deviation and coefficient of variation (CoV) were calculated for the 69 ground measurements in the red and NIR bands. The CoV is a normalized measure of the dispersion of a probability distribution and is defined as the ratio of the standard deviation to the mean. Then the sensitivity of the AFX to view and solar geometries was examined for one ground measurement. Finally, the AFX was assessed for sensitivity to contamination by random simulated noise.

The sensitivity of the AFX to view and solar geometries was examined using a field dataset from a grassland site at the Konza Prairie, KS. The measurements were collected by Deering et al. (1992) using the Portable Apparatus for Rapid Acquisition of Bidirectional Observations of the Land and Atmosphere (PARABOLA) instrument on June 4, 1987 in a ground campaign for the First International Satellite Land Surface Climatology Project (ISLSCP) Field Experiment (FIFE). The data set is comprised of 925 directional observations and 9 solar zenith angles ranging from 18° to 68°. LAI was 2.2; mean canopy height was 35 cm; canopy closure was greater than 90%. The prairie grass site was burned in the spring of the previous year to remove litter. The data set was split into ten random equal-sized subsets that maintained the observation distribution of the entire data set in each subset. Three model parameters and WSA, NDVI and AFX were retrieved for each subset and for the whole data set using the RTLSR algorithm. Average relative difference (ARD) for 10 subsets relative to the whole data set was calculated for all variables.

Sensitivity of AFX to random noise was examined using the same data set (Deering et al., 1992) in four azimuthal planes including principal plane (PP), cross-principal plane (CP), 60° clockwise plane (+60), and 60° counter clockwise plane (−60). The number of the observations in the four planes was respectively 128, 110, 178 and 141. Low values for the WoD (0.00797, 0.01106, 0.00574 and 0.00769) indicated that the spatial distribution of observations along each plane was sufficient to fully capture the surface anisotropy. Random Gaussian noise was generated to contaminate a portion of observations to account for an increasing probability density of Gaussian noise (1/8 and 1/4). The relative difference between each subset and the whole dataset without the noise contamination in that plane was calculated.

2.2.3. Application of AFX to BRDF typology

In theory, the AFX should be able to support a BRDF-based classification scheme for BRDF typology because the AFX reflects the variability of the basic dome-bowl BRDF shapes. The following procedure was adopted to develop a set of AFX-based BRDF archetypes.

(1) The red and NIR AFX values were classified separately to generate different BRDF classes by using the ISODATA (Iterative Self organizing data Analysis technique) Clustering Algorithm.
(2) AFX values were related to model parameters by establishing a look-up table in terms of Eq. (3).
(3) Within-class model parameters (respectively for f_{iso}, f_{vol} and f_{geo}) were averaged to represent archetypal parameters for that class.
(4) Model parameters were then input to the RTLSR algorithm to reconstruct characteristic BRDF shapes.

The ISODATA clustering algorithm uses the minimum spectral distance formula to form clusters, beginning with arbitrary cluster means or means of an existing signature set. Each time the clustering repeats and the means of these clusters are shifted. The new cluster means are used for the next iteration until a given iteration limit or convergence.

To determine how many BRDF archetypes are appropriate for these 69 data sets, the variation of the fit-RMSEs was examined in relation to the number of BRDF archetypes for each of the data sets. First the ISODATA clustering algorithm was used to classify all the AFX of these 69 field measurements into 2–8 BRDF classes for red and NIR bands as indicated above. Then the BRDF archetypes were compared to the corresponding within-class observations to acquire within-class fit-RMSEs. Finally, a mean of these fit-RMSEs was calculated for each case.

2.3. Assessment of AFX with satellite data and model simulations

2.3.1. Satellite data from MODIS

The next logical step was to examine AFX over a wide range of global land cover types. High-quality remotely-sensed MODIS data sets from the EOS LVCS which were intended as a focus for land product validation were used. For the purpose of this study, 26 EOS LVCS were selected to represent a wide variety of vegetation types across global biomes for the year 2004. Although the results from a single year were used in this study, similar results were found when using as many as 5 years. These land cover types were then grouped into broad ecological land cover classes according to a herbaceous-shrub–forest vegetation transition for examination of within-class BRDF variations. These 500 m MODIS BRDF products were used to derive BRDF archetypes that represent a global sample of variation over a one-year cycle. The distribution

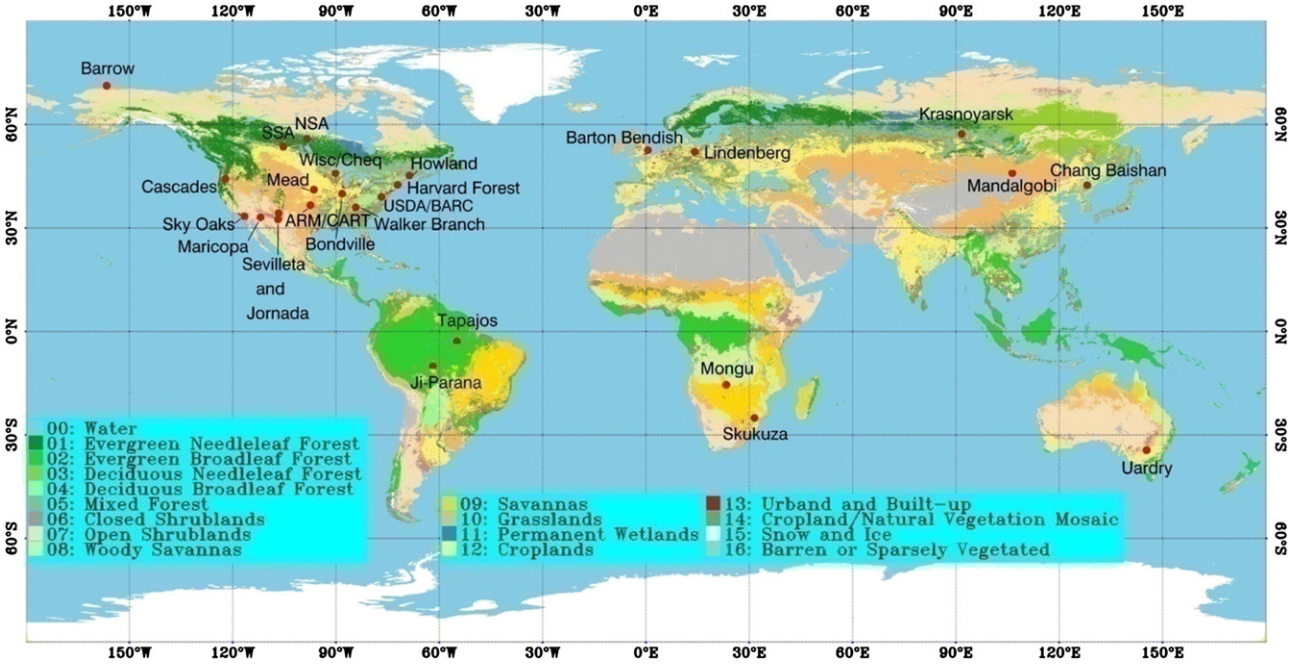

Fig. 2. Distributions of 26 EOS land validation core sites (LVCS) used in this study displayed over the MODIS IGBP land cover classes.

of these 26 EOS LVCS is shown in Fig. 2 and the descriptions of their characteristics are given in Table 1.

The global gap-filled MODIS BRDF/albedo product (in particular the solar zenith angle (SZA)-extended MODIS/Terra + Aqua 30 arc second Global Gap-Filled, Snow-Free MCD43A1 V005 BRDF Parameters Product (MCD43GF)) was used to generate global maps of the BRDF archetypes. The MCD43GF products are global data sets of spatially complete BRDFs computed at seven MODIS bands and three broad bands for 46 retrieval periods per year and are primarily based on the 30 arc second gap-filled snow-free BRDF parameters products (MCD43D) that are, in return, the reprojected average of the underlying 500 m MODIS/Terra + Aqua BRDF/albedo product (MCD43A1), representing the majority quality associated with the underlying data. The MCD43A data product results from a retrieval attempt every 8 days based on a 16 day period. The quality status of each pixel retrieval can be found in the QA (quality assurance) maps.

The MODIS International Geosphere-Biosphere Program (IGBP) classification scheme (Friedl et al., 2002, 2010) was used to evaluate global AFX archetype map produced by high-quality MODIS MCD43GF data. The IGBP classification scheme separates land cover into 16 classes (Fig. 2). The phenology of these 26 EOS LVCS in year 2004 was characterized in terms of their NDVI characteristics, i.e., dormancy, green-up, maturity and senescence based on the approach of Zhang et al. (2003). Consideration of canopy state in certain biomes and hemispheres was very important for the analysis. For example, characterization of AFX archetypes was based on a standard tree canopy state of

Table 1
26 EOS land validation core sites and a broad herbaceous-shrub-forest class. (Mixed land cover represents sites with woody and herbaceous components).

LC	Num	Core sites	DAAC code	Biome	Latitude/longitude	Line/sample	State, country
Herbaceous	1	USDA/BARC	Usdaars	Broadleaf cropland	39.03, −76.85	232.30/72.10	MD, USA
	2	Barton Bendish	Bartonbe	Broadleaf cropland	52.618, 0.524	1771.18/75.35	England, UK
	3	Bondville	Bondvill	Broadleaf cropland	40.0, −88.29	2399.50/566.89	IL, USA
	4	Maricopa	Maricopa	Broadleaf cropland	33.07, −111.97	1662.70/1479.03	AZ, USA
	5	Lindenberg	Lindenberg	Cropland (agriculture)	52.17, 14.12	1878.70/2077.96	Germany
	6	Mead	Mead	Cropland (corn/soy)	41.1651, −96.469	2119.88/1769.70	Mead, NE
	7	ARM/CART	Armcart	Grassland/cereal	36.64, −97.50	805.90/423.17	OK, USA
	8	Mandalgobi	Mandalgo	Grassland/cereal	45.995, 106.327	960.70/927.55	Dundgovi, Mongolia
	9	Sevilleta	Sevillet	Grassland/cereal	34.344, −106.671	1356.94/461.46	NM, USA
	10	Uardry	Uardry	Grassland/cereal	−34.39, 145.30	1053.10/2376.07	Australia
Mixed	11	Barrow	Barrow	Tundra	71.281, −156.612	2092.06/2336.9	Alaska, USA
	12	Jornada	Jornada	Shrubland/woodland	32.60, −106.86	1775.5/2393.0	NM, USA
	13	Sky Oaks	Skyoaks	Shrubland/chaparral	33.377, −116.623	1589.02/626.31	USA
	14	Mongu	Mongu	Shrubland/woodland	−15.438, 23.253	1304.62/578.82	WesternProvince, Zambia
	15	Skukuza	Skukuza	Shrubland/woodland	−25.02, 31.497	1204.30/2048.99	Northern Prov., RSA
Forest	16	NSA	Boreasn	Needleleaf forest	55.87, −98.48	990.70/1138.07	Manitoba, Canada
	17	Wisc/Cheq	Parkfall	Needleleaf forest	45.946, −90.272	972.46/1734.86	WI, USA
	18	Krasnoyarsk	Krasnoya	Needleleaf Forest	57.27, 91.60	654.70/2286.13	Russia
	19	Howland	Howland	Needleleaf forest	45.20, −68.73	1151.50/376.88	ME, USA
	20	Cascades	Cascades	Needleleaf forest (moist)	44.24, −122.18	1381.90/591.17	OR, USA
	21	SSA	Boreass	Boreal forest	53.65, −105.32	1523.50/1816.35	Saskatchewan, Canada
	22	Walker Branch	Walkerbr	Broadleaf forest	35.958, −84.287	969.58/424.88	TN, USA
	23	Chang Baishan	Changbai	Forest (mixed)	42.403,128.096	1822.90/1100.92	Jilin, China
	24	Harvard Forest	Harvard	Broadleaf forest	42.539, −72.178	1790.07/1636.04	MA, USA
	25	Ji-Paraná	Jiparana	Broadleaf forest	−10.08, −61.93	18.70/2165.79	Rondonia, Brazil
	26	Tapajós	Tapajos	Broadleaf forest	−2.857, −54.959	685.18/1225.18	Para, Brazil

leaf-on or leaf-off and the timing of these states varies globally both between and within biomes. Trees in Australian savannas are largely evergreen, but many in African savannas trees lose their leaves to avoid the dry season drought. Hence the phenology data was used to align the canopy conditions for archetype characterization.

2.3.2. Response of AFX to canopy architectures and background

The 5-Scale BRDF model was used to examine the sensitivity of AFX and BRDF archetypes to canopy architectures and background optical properties for three vegetation types with discontinuous woody canopies. The 5-Scale BRDF model is a radiative transfer model that simulates the BRDF in terms of structural and biochemical properties of the vegetation (Chen & Leblanc, 1997). The model includes a multiple scattering scheme that includes all orders of scattering among canopy geometrical structures and has been reported as a reliable simulation tool at a wide range of wavelengths including the near infrared (Chen & Leblanc, 2001; Chen et al., 2005). This simulation includes three cover types (i.e., Conifer, Savanna and Shrub) with very different canopy architectures.

The main input parameters to the 5-Scale BRDF model and their values are given in Table 2. Two geometric representations for the envelope of the tree crown are used. Needleleaf species (Conifer) are modeled using a combination of cylinders and cones (Chen & Leblanc, 1997), while the broadleaved species (Savanna and Shrub) are modeled using full ellipsoids (Li & Strahler, 1992; Strahler & Jupp, 1990). Several papers were consulted for selecting structural parameter values (Chen & Cihlar, 1996; He, Chen, Pisek, Schaaf, & Strahler, 2012; Li & Strahler, 1992; Ryu et al., 2010). The optical reflectance properties of needles/leaves are adopted for the red (0.06) and NIR (0.6) bands. Three background reflectivity values are adopted to represent dark (0.05), gray (0.25) and bright (0.5) soils in the two spectral bands. The tree crown radius (R) is limited by an equation in terms of stem density (ρ) and the vertically projected crown coverage (C), i.e., $10^{-4}\pi R^2\rho \leq C$.

2.3.3. Derivation of BRDF archetypes from MODIS data

An a priori database of BRDF archetypes was established for the four phenological seasons of 2004 for all 7 MODIS bands by using the MODIS BRDF products over the 26 EOS LVCS. To determine how many AFX archetypes were appropriate for these EOS Sites, the procedure described in Section 2.2.3 above for the field data was also applied to the MODIS data. BRDF sensitivity was retained by constructing a sampling scheme for the whole model surface, based on anisotropic measurements at fixed intervals (Sandmeier & Deering, 1999), i.e., azimuth angle interval $\leq$30°, zenith angle interval $\leq$15°. Thus for the MODIS data, the model surface was sampled at intervals of 30° in azimuth angle, 5° in view zenith angle, and for three solar zenith angles (30°, 45° and 60°), within the 70° view and solar geometries recommended as the maximum angles for the RTLSR algorithm (Schaaf, Liu, Gao, & Strahler, 2011).

3. Results

3.1. Analysis of the AFX sensitivity to random noises and observation geometries

Comparison of the CoV among model parameters from the 69 data sets (WSA, NDVI and AFX) shows that AFX appears to be the most stable parameter. The CoV showed a higher level of variation for the model parameters (Table 3). The variation was lower for the NIR band than for the red band for all variables. Among the three model parameters, f_{iso} seems to be most stable since f_{iso} is representative of spectral reflectance at nadir-view and nadir-Sun and is mainly determined by the optical properties of land surface (Roujean et al., 1992).

Model parameters were more sensitive to the variation of view and solar geometries than WSA, NDVI or AFX with $f_{geo} > f_{vol} > f_{iso}$ (Table 3). The AFX however exhibits similar sensitivity to the WSA and NDVI. All variables were more sensitive to different viewing and solar geometries in the red band than in the NIR band.

All variables showed some sensitivity to an increasing proportion of contaminated observations (Table 3). The BRDF principal plane exhibits less sensitivity to an increasing proportion of noise than other planes (except for NDVI). Noise sensitivity did not differ greatly between the red and NIR bands. Model parameters were more sensitive to random Gaussian noises than other variables, with f_{iso} the least sensitive. The sensitivity of f_{vol} and f_{geo} to noise contamination may arise from the fact that volumetric scattering and geometric-optical kernels are not necessarily orthogonal (Lucht et al., 2000). The invalid values (null) for f_{geo_nir} in cross-principal plane are caused by the constraining technique.

3.2. Analysis of the additional information contained in the AFX

The NDVI may be the most widely used spectral vegetation index that was mainly used for land cover classification in early research (e.g., Defries & Townshend, 1994; Hansen, Defries, & Townshend, 2000). Although the NDVI was not designed to consider angular scattering, several studies (e.g., Bréon & Vermote, 2012; Vermote, Justice, & Breon, 2009) have recently suggested that NDVI is linearly related to individual MODIS BRDF parameter (f_{vol} or f_{geo}) and therefore can be used to develop a general approach for MODIS BRDF correction. To explore this assumption, a comparison of AFX with NDVI was made in order to distinguish the structural scattering information captured by AFX that is independent of the reflectance magnitude response captured by NDVI, as well as explore the difference in using the indices rather than directly using individual model parameters. Comparison of the AFX and NDVI values (Fig. 3) for the 69 field site measurements demonstrated that for any given NDVI observation AFX values exhibit a large dynamic range. The correlation between AFX and NDVI was significant but modest ($R_{red} = 0.595$ and $R_{NIR} = 0.476$). Thus this range in AFX values reflects the intrinsic differences in both the spectral and directional sensitivities to different land surface properties. Therefore, for a specific NDVI value, AFX will exhibit a range of values that reflect additional differences related to canopy physiognomy and structure (e.g., canopy height, size, within-crown gaps vs. between-crown gaps, and background vs. foliage contributions).

The NDVI-axis (Fig. 3) is divided into four major regions according to the stratification of the NDVI response to broad scene components (Holben, 1986): soil (0.025–0.09), light green-leaf vegetation (0.09–0.14), medium green-leaf vegetation (0.14–0.50) and dense green-leaf vegetation (>0.50). If the AFX axis is similarly divided into four major zones based on strong bowl shapes (AFX > 1.11/1.12), slight bowl shapes (AFX 0.96/0.98–1.11/1.12), slight dome shapes (AFX 0.78/0.79–0.96/0.98) and strong dome shapes (AFX < 0.78/0.79) according to the BRDF classes in Section 3.3 below, then the important variation

Table 2
Input parameters to 5-Scale and their values used in modeling.

Cover type	Tree envelop shape	Tree clumping		Shape parameter (m)			Leaf area index	Foliage clumping	Vertical crown coverage (%)	
		Number	Nyman	Stick height	Crown height	Crown radius			low	high
Conifer	Cone/cylinder	30	4	0.5	6.5	0.75	2.5	0.65	0	60
Savanna	Full ellipsoid	5	4	2	10	3.0	1.5	0.70	0	60
Shrub	Full ellipsoid	30	4	0	1	0.5	1.5	0.75	0	60

Table 3
Analysis of AFX sensitivity, response to geometry and response to random noise relative to other variables.

	f_{iso_red}	f_{vol_red}	f_{geo_red}	f_{iso_NIR}	f_{vol_NIR}	f_{geo_NIR}	WSA $_{red}$	WSA_{nir}	NDVI	AFX $_{red}$	AFX_{nir}
Sensitivity											
Mean	0.106	0.050	0.016	0.313	0.170	0.029	0.094	0.305	0.552	0.978	0.980
Std	0.097	0.041	0.021	0.100	0.107	0.032	0.080	0.108	0.271	0.205	0.156
CoV	0.912	0.819	1.337	0.319	0.627	1.094	0.851	0.353	0.491	0.209	0.159
Geometry											
Mean Sub_{01-10}	0.100	0.046	0.009	0.273	0.158	0.008	0.097	0.291	0.485	0.967	1.068
ARD(%)	3.850	12.01	29.75	1.610	5.390	24.39	1.620	0.840	1.140	3.620	1.180
Random noise											
PP (1/8)	2.45	8.019	12.47	2.63	8.051	30.84	1.52	1.54	1.02	1.18	1.35
PP (1/4)	2.51	10.40	11.69	2.59	11.25	31.25	1.82	1.74	1.48	1.32	1.57
CP(1/8)	3.84	21.34	38.88	4.49	11.48	Null	1.49	1.58	0.16	2.92	3.42
CP(1/4)	11.0	59.64	89.55	12.1	34.62	Null	5.60	5.67	0.42	7.17	7.97
+60(1/8)	1.24	11.67	12.68	1.28	6.95	39.00	0.85	0.89	0.25	1.10	1.17
+60(1/4)	6.49	36.57	50.88	7.61	21.48	160.1	2.28	2.19	0.44	4.49	5.56
−60(1/8)	3.16	9.52	16.14	3.81	7.95	138.8	1.14	1.04	0.22	2.24	2.94
−60(1/4)	6.44	26.50	30.52	7.96	21.27	266.6	3.19	3.17	0.47	4.00	5.18

associated with high and low NDVI is highlighted. There is a wide variation in red AFX above NDVI of 0.67, and significant variation in NIR AFX below NDVI of 0.22.

3.3. Application of AFX to BRDF typology for the 69 field sites

The variability in fit-RMSE against number of BRDF archetypes is shown in Fig. 4. The fit-RMSE reaches a stable asymptote at four BRDF archetypal shapes and accounts for >95% of total fit-RMSE (right subplot of Fig. 4), with RMSEs reduced to ~0.019 in red band and ~0.045 in NIR band. The 69 BRDF shapes in the principal plane (PP) in the red and NIR bands with each color representing the same BRDF classes are shown in Fig. 5 (top).

These BRDF shapes don't present distinctly regular variability because of the difference in spectral reflectance amplitude of land covers as determined by the model isotropic parameters (f_{iso}). This spectral reflectance difference is removed by normalizing the BRDF shapes by multiplying them by a scale factor $K = \alpha/f_{iso}$. This applies the same method as used for AFX definition (therefore such normalization represents an "AFX transform" for both model parameters and reflectance). Here, α is an adjustment factor to limit the range of the adjusted shapes. We take $\alpha = 0.5$ to force most shapes into 0–1.0 range in this study. An $\alpha = 1$ is used to retain original AFX values. The 69 normalized BRDF shapes in red and NIR bands are shown in Fig. 5 (bottom) with the same color codes. The normalized shapes now represent a gradient of dome-to-bowl variability, indicating a distinct transition from geometric-optical scattering to volumetric scattering compared with their original form. The four BRDF archetypes for red and NIR together with within-class BRDF variation are qualitatively demonstrated in Fig. 6 (solid curves represent BRDF archetypes and dashed curves represent the variation of within-class BRDF shapes around the BRDF archetypes). These BRDF archetypes (bold solid curves) show a change from dome to bowl shapes that corresponds with the AFX values changing from less-than-unity to greater-than-unity. The corresponding AFX values for both the red and NIR represent unique BRDF types.

The original and normalized model parameter values and AFX threshold values for the four archetypes as derived from the 69 field sites are provided (Table 4). Table 4 also quantifies the within-archetype variation by calculating the standard deviation of AFX. The wider dynamic range of AFX in the red band represents more variability in BRDF shapes. Within-archetype standard deviations are larger for the low and high values of the AFX archetypes, since these archetypes include the more extreme AFX values associated with extreme dome and bowl shapes. In general, the maximum within-archetype fit-RMSE retains ~0.025 in red and ~0.055 in NIR for individual BRDF class that has the highest within-class variances. This indicates that the maximum within-archetype fit-RMSE is fairly stable and the information content of the extreme types is generally preserved in the AFX-classification process with the ISODATA algorithm. The normalized model parameters illustrate regular variability, i.e., for a constant f_{iso}', increasing f_{vol}' implies increasing

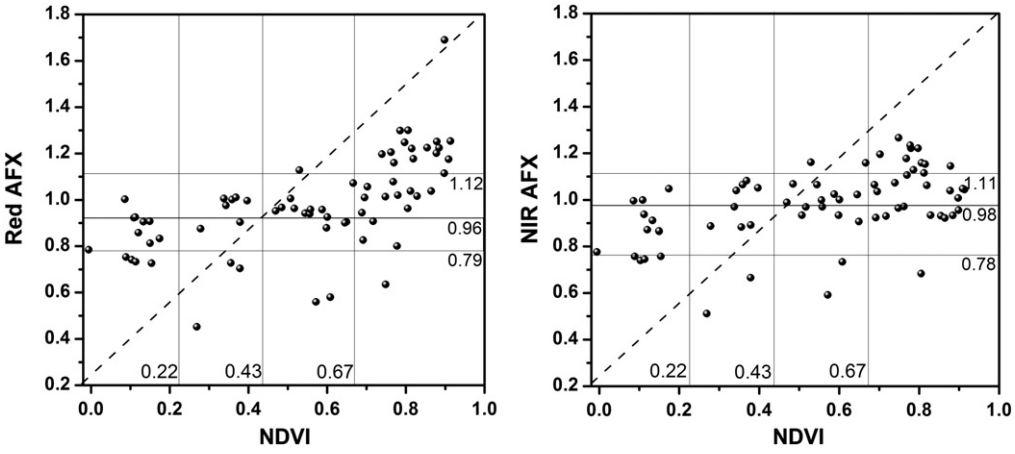

Fig. 3. The scatter plots of the NDVI vs. AFX for 69 measurements in red and NIR bands.

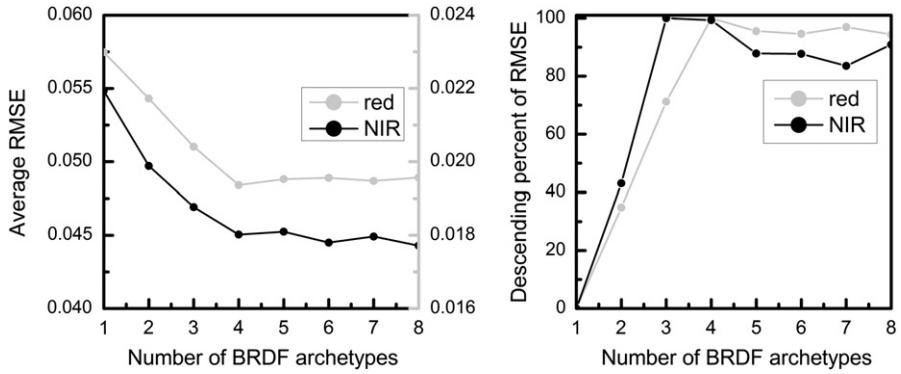

Fig. 4. Variability in fit-RMSE against the number of BRDF archetypes in red (left) and NIR (right) bands.

weights of volumetric scattering, and decreasing f_{geo}' implies decreasing weights of geometric-optical scattering, matching the variability of dome-to-bowl BRDF shapes.

To relate the AFX archetypes to actual vegetation and land surface characteristics, the archetype classes are described in terms of the available field site descriptions, fractional vegetation cover (FVC) if known or estimated for unknown data using an algorithm (Roujean & Lacaze, 2002), and a conceptual representation of the scattering characteristics (volume and geometric-optical) for the red (Table 5) and NIR (Table 6) bands. In general, the BRDF archetypes change from dome to bowl with increasing FVC, implying an increasing volume scattering and decreasing geometric-optical scattering as a canopy becomes more closed. For both red and NIR, soil types with different textures represent purer dome shapes, while the dense vegetation locations with high FVC represents purer bowl shapes. There is some variability in the site descriptions (Tables 5, 6) within the AFX archetypes 2 and 3. This suggests that more precise model simulations may be needed at a site level to further understand the response of AFX values to canopy architectures and background optical properties especially for vegetation with discontinuous canopies.

3.4. Assessment of the AFX with satellite data and model simulations

3.4.1. Comparison of AFX with NDVI for the MODIS data

The AFX from the MODIS BRDF MCD43A1 product for red and NIR bands is compared to the NDVI for the North America region using only high-quality full-inversion retrievals (Fig. 7). The results show a very large variation in AFX values for a given narrow band of NDVI values associated with a broad land cover class. The first two principal components derived by the principal component analysis (PCA) are plotted as black lines across the scatter plot. Although more of the overall variation is explained by NDVI since PC_1 (65%) is almost horizontal

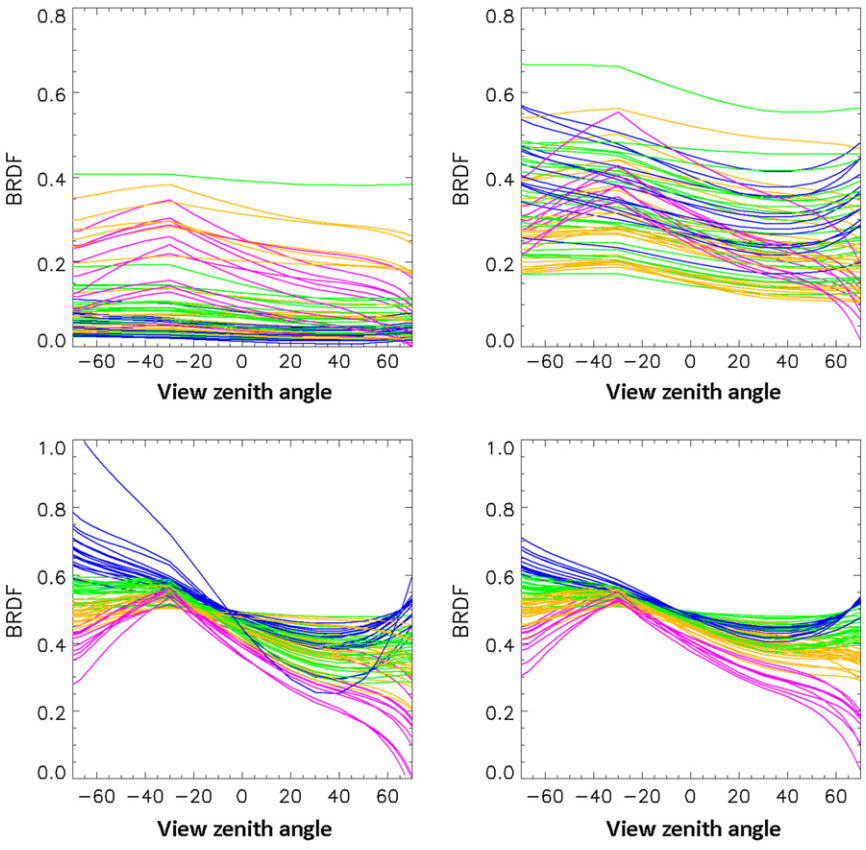

Fig. 5. 4 BRDF classes derived from 69 BRDF shapes of ground measurements with each color representing the same BRDF class in the original (top) and normalized (bottom) fashions.

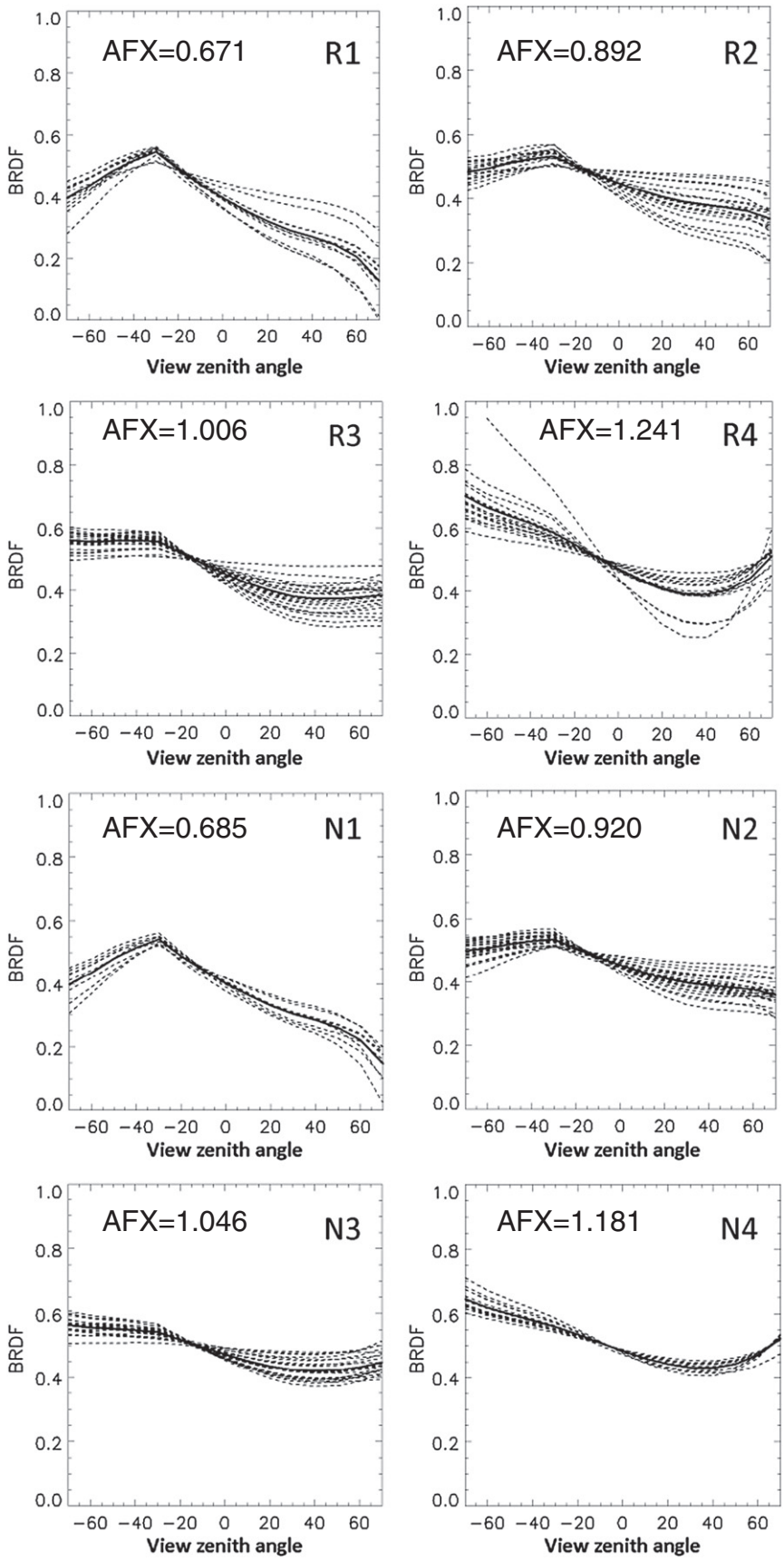

Fig. 6. 4 BRDF archetypes (solid curves) and within-class BRDF shapes (dashed line) in red (R1, R2, R3 and R4) and NIR (N1, N2, N3 and N4) bands.

Table 4
AFX and 4 BRDF archetypal parameters in original and normalized forms for 69 field measurements in red and NIR bands.

band	AFX range	AFX mean	AFX_{std}	f_{iso}	f_{vol}	f_{geo}	f_{iso}'	f_{vol}'	f_{geo}'
Red	[0.45,0.79]	0.671	0.103	0.2039	0.0704	0.0552	0.50	0.1760	0.1429
	[0.80,0.95]	0.892	0.046	0.1316	0.0370	0.0160	0.50	0.2050	0.0668
	[0.96,1.08]	1.006	0.036	0.0873	0.0534	0.0072	0.50	0.3744	0.0470
	[1.11,1.69]	1.241	0.127	0.0395	0.0544	0.0011	0.50	0.7311	0.0106
NIR	[0.51,0.78]	0.685	0.086	0.3618	0.0927	0.0937	0.50	0.1367	0.1290
	[0.87,0.97]	0.920	0.045	0.2865	0.1057	0.0309	0.50	0.2121	0.0564
	[0.99,1.11]	1.046	0.031	0.3176	0.1834	0.0157	0.50	0.3048	0.0271
	[1.13,1.27]	1.181	0.045	0.3389	0.3253	0.0006	0.50	0.4871	0.0015

and parallel to the NDVI axis, significant variation is explained by PC_2 (35%) which is almost vertical and parallel to the AFX axis. Again, it is important to note that although several studies have suggested that NDVI is linearly related to the individual MODIS BRDF parameter, i.e., f_{vol} or f_{geo} (e.g., Bréon & Vermote, 2012; Vermote et al., 2009), our finding demonstrates that the AFX (based on geometric and volume parameters normalized to remove the spectral reflectance amplitude) is approximately orthogonal to NDVI, especially for MODIS data, and contains additional important information related to vegetation structure as is demonstrated in Section 3.4.3 below.

3.4.2. Derivation of BRDF archetypes from MODIS data

The MODIS data from the 26 EOS LVCS covered more of the potential global variation in vegetation and land surface structure than was available from the 69 field sites (Table 1). As a result, the analysis (with the same methods as applied to the field site data above) indicated that 6 archetypes, somewhat depending on different phenology and different bands, were sufficient to represent the potential BRDF shapes for MODIS reflectance data in each of four phenological seasons, and also over the entire whole year (Fig. 8). We must note that the RMSE values derived in this way have smaller values than using real observations since the random errors of observations have already been smoothed out by model; therefore, the RMSE values between the BRDF archetypal surface and each within-class model surface mainly reflect the discrepancy between the two models. Fig. 8 indicates that as the number of BRDF archetypes increase, the discrepancy between two model surfaces decreases and accounts for >80% of the total fit-RMSE for 6 archetypes (right lower subplot), indicating that there are sufficient BRDF archetypes to describe the observed variation.

Fig. 9 shows 6 BRDF archetypes for each MODIS band. The annual archetypes are also representative of the seasonal phenological archetypes derived (data not shown). However the seasonal archetypes showed greater dynamic variation with the values from the maturity season being greater than those from the dormancy season, and the green-up and senescence seasons showing intermediate values. The BRDF archetypes are somewhat band-dependent with visible bands capturing a wider range of dynamics than the NIR bands. Although the BRDF archetypes are also somewhat phenology-dependent, the archetype-to-archetype fit-RMSEs for the model surface between the entire one year period and each of the four phenological seasons approximates to ~0.004 at 30° solar zenith angle, indicating that 6 one-year BRDF archetypes are appropriate to represent the generalized anisotropy of vegetated surface in the 7 MODIS bands at the global scale. Within-archetype variation (data and shapes) is not presented here due to space limitations, but the same quantitative framework to qualify the representativeness of the archetypes was applied to the MODIS data.

3.4.3. Response of AFX to canopy architectures and background optical properties

Simulations with the 5-Scale BRDF model demonstrate that there is significant variation in the response of the AFX to variation in canopy architectures, background optical properties, and canopy cover between the red and NIR bands (Fig. 10). The response to the crown coverage of woody vegetation is non-linear, and differs between the spectral bands depending upon vegetation type. The response observed (Fig. 10) indicates that scattering processes within canopy radiative regime change when canopy architecture and background optical properties change. For the NIR band, there is mainly an increasing trend in the AFX_{NIR} value with increasing crown coverage (thus stem density) for the three cover types indicating that the volume scattering increases with the crown coverage of vegetation canopy.

For the red band, the response of AFX_{red} to crown coverage is more complex. There is first a decreasing trend in the AFX_{red} with crown coverage for all soils and vegetation types, and then a transition to an increasing trend in the AFX_{red} for dark soil alone (and somewhat for Conifer with two other soils as well). Such a "bowl shape" response in AFX_{red} to crown coverage reveals an increasing geometric-optical scattering response first, followed by an increasing volumetric scattering with increasing crown coverage. The location of the changeover points in the "bowl shape" response somewhat relies on the vegetation types.

AFX values are sensitive to stem density although the overlapping range of stem density for three types is not enough to allow a complete analysis (Fig. 10a–c). The soil effect on the sensitivity of AFX values reveals a trend of slow increase with crown coverage. This can be seen through the discrepancies between the different soils for the same vegetation type with crown coverage. Although we cannot separate vegetation structure communities (stem density, crown shape, crown size, tree high and foliage clumping) as was used in the simulation, since real vegetation stands are being evaluated, the general response of AFX to these structural associations can be analyzed through calculation

Table 5
Descriptions of BRDF archetypal classes derived from 69 measurements in red band. FVC indicates fractional vegetation cover.

BRDF class (num)	AFX range (mean)	FVC	Data source	BRDF class descriptions
1 (10)	0.45–0.79 (0.671)	0	Soil textured (Irons et al., 1992); plowed field (Kimes, 1983); rock strewn land (Deering et al., 1992)	Very strong scattering from discrete crowns/objects
		0.32–0.80	Sowing-in-row Crops (Leroy & Bréon, 1996 for air-borne POLDER; Ranson et al., 1985); dense buildings (AVHRR)	
2 (23)	0.80–0.95 (0.892)	0	Bare soil/lava (Deering et al., 1992)	Major scattering from discrete crowns/objects
		0.11–0.74	Open or sparse grass or crops (Kimes, 1983); Tiger Bush (air-borne ASAS); vegetable (Leroy & Bréon, 1996 for air-borne POLDER)	
		0.12–0.51	Sparse bushes on light background (Deering et al., 1999, 1992); major sparse clumping trees (BOREAS);	
3 (23)	0.96–1.08 (1.006)	0	Bright soils/alkali flat (Deering et al., 1992)	Lambertian surface
		0.12–0.76	Major sparse uniform grass (Kimes et al., 1985; FIFE); cerrado (Tsay et al., 1998 for air-borne SCAR)	Major scattering from leaf-layer type
		0.21–0.73	Sparse-to-dense uniform clumped-foliage trees (Deering et al., 1999, 1994; BOREAS)	
4 (13)	1.08–1.69 (1.241)	0.60–0.98	Dense layered crops or grass (Kimes, 1983; Kimes et al., 1985; Ranson et al., 1985 BOREAS)	Very strong scattering from leaf-layer type
		0.73–0.89	Dense layered tree (Kimes et al., 1985; Tsay et al., 1998 for air-borne SCAR; BOREAS)	

Table 6
Descriptions of BRDF archetypal classes derived from 69 measurements in NIR band. FVC indicates fractional vegetation cover.

BRDF class (num)	AFX range (mean)	FVC	Data source	BRDF class descriptions
1 (10)	0.50–0.78 (0.685)	0	Soil textured (Irons et al., 1992); plowed field (Kimes et al., 1985); rock strewn land (Deering et al., 1992);	Very strong scattering from discrete crowns/objects
		0.32–0.80	Sowing-in-row Crops (Leroy et al. for air-borne POLDER; Kimes, 1983); dense buildings (AVHRR)	
2 (23)	0.87–0.97 (0.692)	0	Bare soil (Deering et al., 1992)	Major scattering from discrete crowns/objects
		0.11–0.68	Sparse or open grass (Kimes, 1983; Vierling et al., 1997); Tiger Bush (air-borne ASAS); sparse woodland (Tsay et al., 1998 for air-borne SCAR)	
		0.12–0.86	Sparse bushes (Kimes, Newcomb, Nelson, & Schutt, 1986); major sparse clumping trees (BOREAS); other dense trees	
3 (23)	0.99–1.11 (1.046)	0	Bright soils/alkali flat (Deering et al., 1992)	Lambertian surface
		0.14–0.98	Sparse-to-dense uniform grass or crops (Kimes, 1983; FIFE)	Major scattering from leaf-layer type
		0.40–0.89	Sparse-to-dense uniform clumped-foliage trees (Deering et al., 1999; BOREAS)	
4 (13)	1.13–1.27 (1.181)	0.60–0.90	Dense layered crops or grass (Kimes et al., 1986; Ranson et al., 1985; BOREAS)	Very strong scattering from leaf-layer type

of the standard deviation of three vegetation types for same soil brightness. Fig. 10d shows that the vegetation structural associations are more sensitive to AFX values at the low-to-moderate range of crown coverage. However, further investigation into the potential definite relationship between the AFX and individual vegetation structural parameter obviously needs more substantial simulation, modeling and validation.

The numbered AFX zones separated by dashed lines in both bands represent the BRDF archetype classes. Obviously, there is a wider response of BRDF archetype class to canopy architecture and background optical properties. In the red band, such responses are mainly confined to 2–3 archetype classes for discontinuous vegetation indicating a major between-crown surface scattering type. In the NIR band, such responses expand to more archetype classes (2–5 archetypes) demonstrating the increased importance of within-crown volume scattering type. Again, in both bands, such responses appear to be more sensitive to dark soil than the two other soils.

3.4.4. Analysis of within-class variation of BRDF archetypes

Since AFX has been shown to be responsive to both canopy condition and background optical properties in the preceding section, the association between land cover types and AFX archetype class for the phenological seasons is worth exploring (Fig. 11). The data show the number of pixels associated with each archetype split into herbaceous, mixed, and forest cover types. The variation in total numbers is determined by the number of pixels available from the MODIS BRDF/Albedo with the best QA flag, a number which is different in four the phenology seasons due to cloud cover and atmospheric factors. There is significant variation in the pixel number among all the land cover types and across all phenological seasons; therefore, the percent of ecological biome within each archetype is calculated for direct comparison. While many of the EOS LCVS have non-uniform and/or non-typical land cover within the area of a single 500 m MODIS pixel, there are, nevertheless, some patterns that significantly relate to the AFX archetype classes.

In general, there is no ecological biome exceeding 50% within each archetype class, revealing the ecological biomes under investigation and BRDF archetype classes need not coincide. Herbaceous sites are predominantly split among red archetypes 1–4 during dormancy, but with a shift more towards archetypes 4 and 5 at green-up and maturity, and back to archetypes 3 and 4 during senescence (Fig. 11). For herbaceous sites, the NIR archetypes 3–5 predominate during dormancy, but the pattern shifts towards archetypes 4–6 in green-up and maturity, and is highly variable during senescence. This pattern is consistent with a sequence moving from soil and stubble, to mixed soil and green canopy, to closed full canopy from dormancy to maturity, and finally to a spatial mosaic of temporal patterns of harvested crops with stubble and soil remaining during senescence.

Forest sites are also split among the red archetypes 1–4 during dormancy and tend to be increasingly dominated by archetypes 3–6 during green-up and maturity, but have variable archetype associated with senescence. The NIR archetype 1–2 predominates during dormancy and senescence, but sites are divided among the archetypes at green-up and maturity. This suggests that there is significant variation in gap fractions and background optical properties between leaf-on and leaf-off condition over an entire MODIS pixel among the forest sites.

The mixed sites showed a more complex phenological behavior for the red and NIR archetype associations, but archetypes 2–4 tended to alternately predominate in all phenological stages. It would be expected that these sites correspond with the archetypes where AFX is highly sensitive to more variability in fraction of tree canopy and background properties in relatively open two layer vegetation types. This

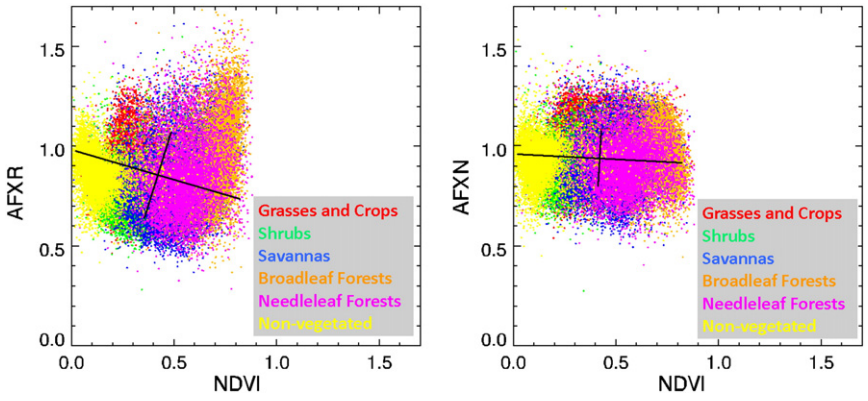

Fig. 7. Scatter plots of NDVI vs. AFX in July (day 185) for the red and NIR bands (values of NDVI < 0 are omitted).

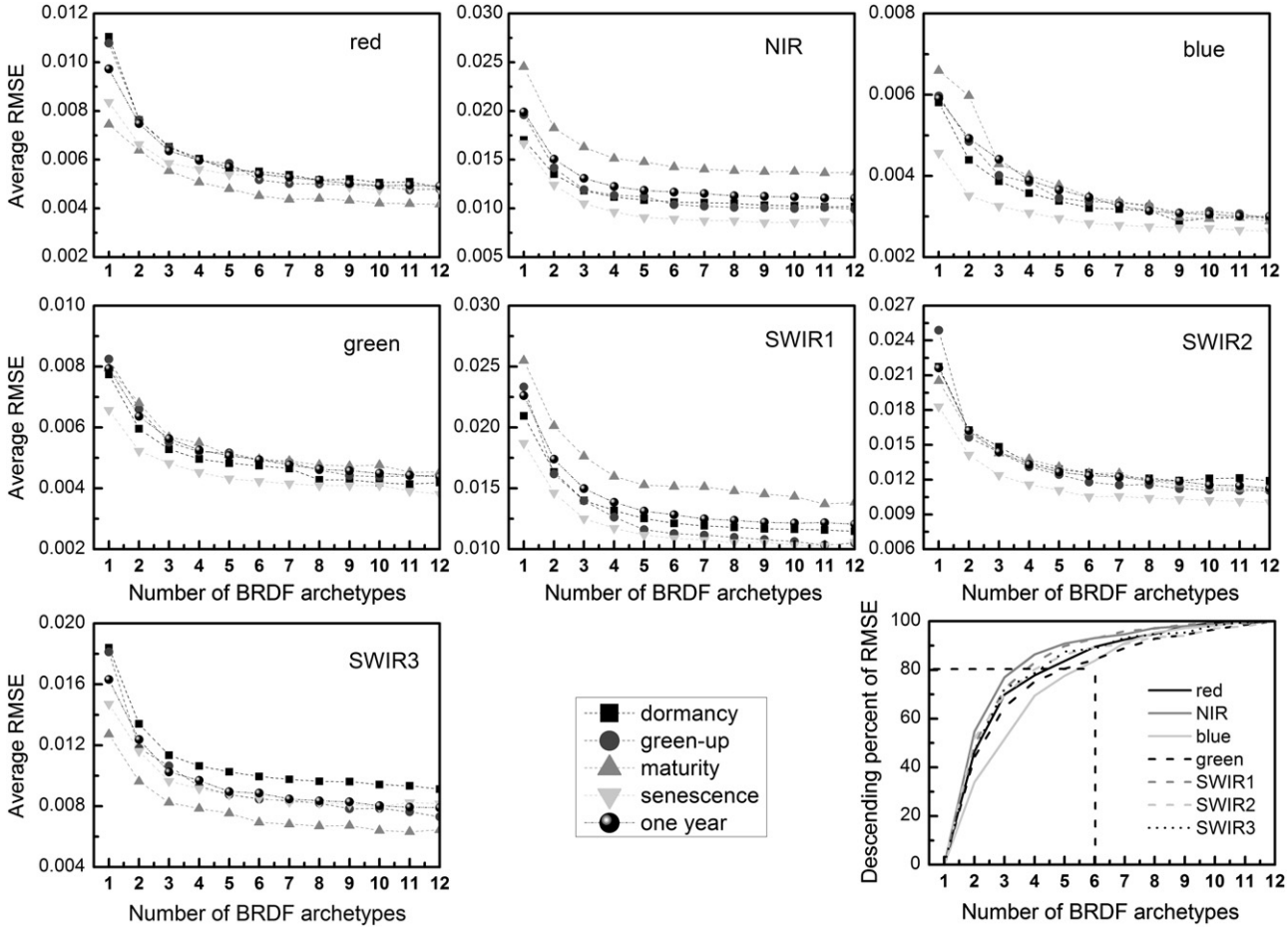

Fig. 8. Fit-RMSEs against the number of BRDF archetypes for four phenological seasons and one year (2004) in 7 MODIS bands at 45° solar zenith angle.

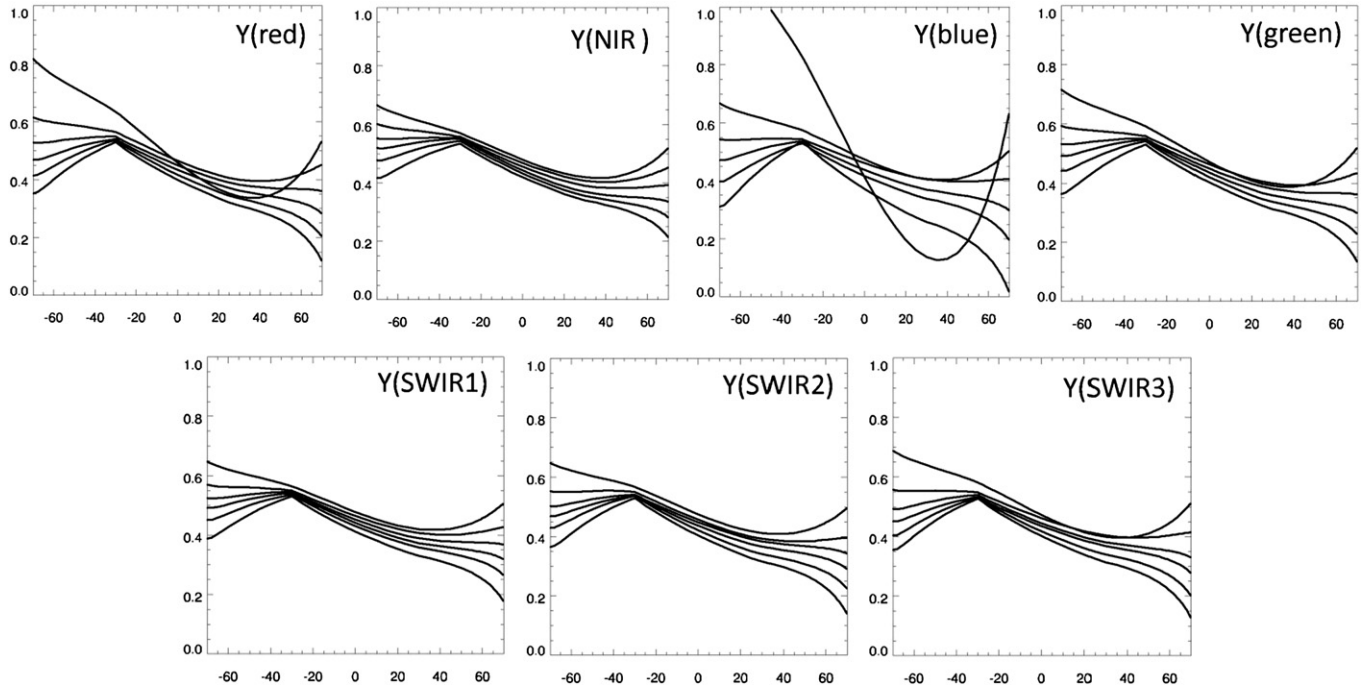

Fig. 9. Plots showing the 6 annual BRDF archetypes for the seven MODIS bands: red (620–670 nm), NIR(841–876 nm), blue (459–479 nm), green (545–565 nm), SWIR1 (1230–1250 nm), SWIR2 (1628–1652 nm) and SWIR3 (2105–2155 nm).

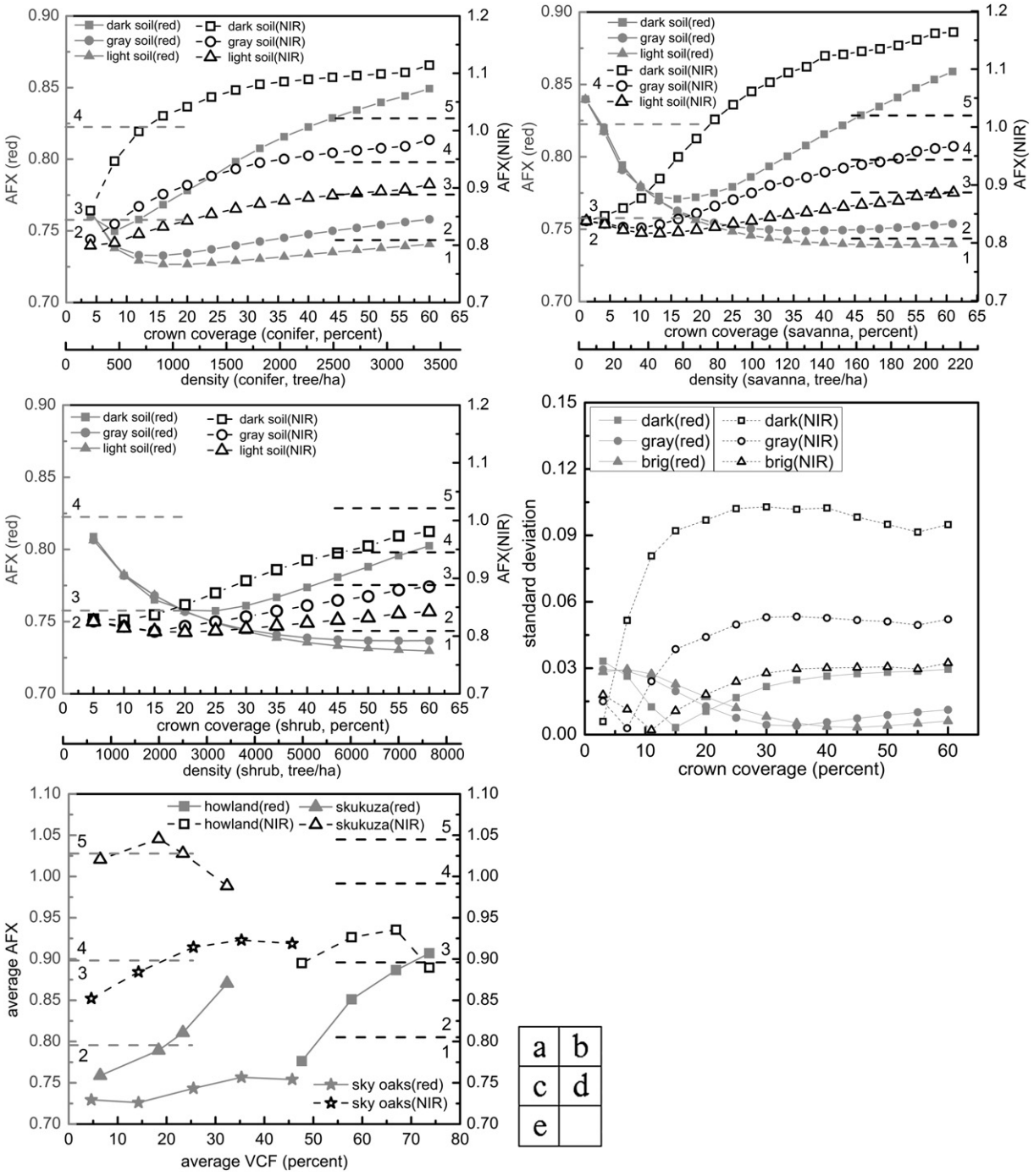

Fig. 10. Response of AFX to canopy architectures (size, shape and spacing) and background optical properties (dark, gray and bright soils) for three discontinuous vegetation canopy in red (left vertical axis) and NIR (right vertical axis) bands for Conifer (top), Savanna (middle) and Shrub (bottom). The numbered AFX zones separated by dashedlines in both bands are BRDF archetype class.

investigation is basically consistent with the result of the 5-Scale BRDF model simulation although these global EOS sites have more complex heterogeneous environments (e.g., a variety of land covers, different phenological processes and unstable background properties).

3.4.5. Global characterization of BRDF archetypes

The global pattern of red and NIR AFX archetypes for January and July in the year 2004, is shown in Fig. 12 along with the distribution of QA flags. The red and NIR bands capture the major photosynthetic responses. An assessment of the QA flags (Fig. 12a) showed that tropical regions in Africa, South America and South East Asia have the greatest reduction in data quality principally due to cloud. High-quality full-inversion retrievals (QA = 0 and 1) accounted for only 9.8% in January, 48.3% in April, 68.8% in July and 12.4% in October. If the temporally fitted pixels (QA = 2), for which a phenological temporal curve fitting exercise has been performed, are also treated as an acceptable quality flag, the areas become 22.3% in January, 86.4% in April, 97.2% in July and 21.3% in October.

In order to examine within-class variability in relation to the AFX and BRDF archetypes, we first perform a quantitative analysis of the ~25 km^2 areas surrounding three EOS sites (Howland, Skukuza and Sky Oaks). These regions have purer IGBP classes corresponding to Evergreen Needleleaf Forest (Conifer), Savanna and Shrub (http://landval.gsfc.nasa.gov/coresite_gen.html) similar to what was used in the

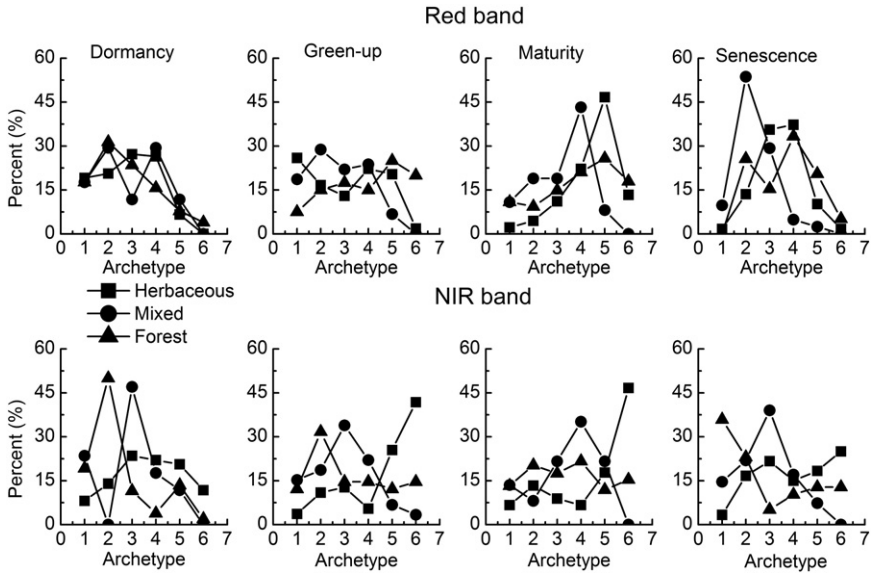

Fig. 11. Within-class variations of BRDF archetypes (in percent) related to a broad ecological biome of Herbaceous, Mixed and Forest over 26 EOS LVCS.

model simulation. The vertical crown coverage is approximated by the fractional coverage of woody cover extracted from MODIS MOD44B Vegetation Continuous Field (VCF) product that provides global fractional cover estimation for trees, herbaceous plants and bare soil (Hansen et al., 2003, 2002). To remove possible noise and fill the gaps, the available AFX values on three continuous DOYs were averaged for Howland (089, 097, 105), Skukuza (089, 097, 105) and Sky Oaks (169, 177, 185). During this time, there is not an obviously herbaceous background in Howland and Sky Oaks. At Skukuza, the trees are still in a mostly full leaf state, while in the grass layer blades have begun to senesce and detach (Archibald & Scholes, 2007). The values in the average AFX image, as well as the corresponding VCF values, are then averaged respectively in terms of 10% of VCF slices. The response of AFX to VCF for these three regions is examined (Fig. 10e).

As was examined in the 5-scale model simulation, the AFX is generally sensitive to the VCF and distinctly differs between red and NIR. AFX_{red} generally displays an increasing trend, while AFX_{NIR} seems to be saturated for Sky Oaks, but decreases for Howland and Skukuza at the higher VCF ranges. The difference between the model simulation and the real data most probably comes from more complex heterogeneous environments and background of the three areas surrounding these EOS sites. In general, these three regions are classified into archetype 2–3 for AFX_{red}, but into archetype 3–4 for AFX_{NIR} (Fig. 10e). This result concurs with the 5-scale model simulation results.

An extensive qualitative analysis of the maps of AFX archetype distribution shows a high level of spatial heterogeneity in the geographical patterns within regions (Fig. 12) indicating that the archetypes are representing directional information that is not captured by NDVI maps (not shown here due to space limitation) or the IGBP map (Fig. 2) alone. If the MODIS band patterns are examined for the key channels in turn, several major features are evident from the maps. Within the tropics, South American, African, and SE Asian forested areas exhibit consistent associations with red archetype 3 and NIR archetype 4. Saharan Africa and Arabia shift from red archetype 5 in January to flat archetype 4 in July (Fig. 12b). There is a similar variation in the spatial pattern of NIR archetypes in these areas, but from the 5/4 archetypes to 3 archetype. A distinct area of NIR archetype 1 (strong dome shape) is seen across the south-western USA, Mexico, the coastline of the Mediterranean and the Red Sea, and through Eurasia to SE Asia and China in January (Fig. 12c). By contrast a significant band of NIR archetype 6 (strong bowl shape) stretches across the north-central areas of North America and Europe, Russia into China, likely corresponding to active agriculture (Fig. 12c).

The variation between the IGBP class and BRDF archetype class can be more easily examined in a desert ecoregion (e.g., Sahara Desert) where within-class BRDF archetypes change with space and season (Fig. 12). Archetypes 3–5 are predominant in the red and NIR in this desert ecoregion indicating primarily Lambertian and slight bowl/dome shapes (a few extreme domes as well). This is most probably due to the somewhat heterogeneous environments in this desert ecoregion (e.g., sand dunes, stone plateaus, gravel plains, dry valleys and salt flats) as well as seasonal migration of vegetation associated with the change of zonal wind and specific humidity in Northern Africa (Harada, Sumi, & Ohmori, 2003).

4. Discussion

In this study, a new anisotropic flat index (AFX) was developed using both ground measurements and satellite observations from MODIS. The AFX characterizes the variability of dome-to-bowl anisotropic reflectance patterns. An AFX <1 shows that geometric-optical surface-scattering effects are dominant, indicating a dome-shaped anisotropic reflectance pattern with a prominent backscatter reflectance peak being located in retro solar view angle. An AFX >1 shows that volume-scattering effects are dominant, indicating a bowl-shaped reflectance asymmetry where reflectance near nadir is lower than for larger scattering angles with the minimum usually displaced towards the forward scattering direction in principal plane. An AFX $= 1$ reveals that geometric-optical surface-scattering counteracts volumetric scattering, indicating an approximately flat BRDF shape. The AFX is not sensitive to observation geometries and noise contamination when there are sufficient observations to adequately sample the viewing hemisphere. This implies that the BRDF shapes indicated by the AFX are stable and are able to resist random noise contamination.

There was moderate correlation between the NDVI and the AFXs in red and NIR bands (~0.6 and ~0.5) for field data. However, the comparisons for satellite measurements from MCD43GF over a range of biome types at global scale using a PCA technique demonstrate that the AFX is approximately orthogonal to NDVI. The 5-Scale BRDF model simulation further demonstrates that the AFX is mainly driven by the sensitivity of land surface intrinsic properties to directional signatures in relation to land surface structures.

The AFX supports a BRDF-based classification scheme for BRDF typology. The classification results in a defined set of AFX archetypes for each of the seven spectral channels in the MODIS BRDF product. As a result, the major development from this study lies in the derivation of a

consistent BRDF typology with discrete AFX archetypes representing major variability of BRDF shapes across the full range of structural variation. BRDF shapes derived from approximating BRDF models generally don't appear to be distinctly separate because regular BRDF effects are confused by the reflectance amplitudes determined by model isotropic parameter. The AFX normalizes the anisotropic reflectance pattern, and thus provides a basis for clearly characterizing BRDF shape, and therefore clearly defining BRDF types in a way that is directly connected to structural change. Extensive analyses showed that four BRDF archetypes could be derived from 69 collected field measurements. However, with a more comprehensive coverage of land cover types and seasonal change, approximately 6 BRDF archetypes were sufficient to represent the anisotropic reflectance pattern at a global scale over the full range of biome types.

An extensive analysis of the maps of AFX archetype distribution demonstrates BRDF archetype classes and ecological biomes under investigation need not coincide. Global mapping of these archetypes revealed substantial fine scale variation, with some broad geographic patterns of archetypes and groups of archetypes. Analysis of the frequency distributions of AFX archetypes within MODIS IGBP land cover classes for both NH and SH showed that while there are consistent patterns of archetype dominance and changes in dominance between seasons, there is also a large amount of variation in archetypes within classes due to structural variations, and significant structural information may be available from AFX archetypes from SWIR channels. This will have to be explored in the future.

The key information content embedded in the AFX archetypes lies in the relationship between the BRDF typology and surface condition. The 5-Scale BRDF model simulation demonstrates that the continuum in BRDF shape from dome to bowl reflects a non-linear response to the change in surface properties from major scattering from discrete objects through a smooth surface to major scattering from dense continuous leaf-canopies. The maps of archetypes and the frequency distributions of archetypes within land cover types and hemispheres reveal substantial fine scale variation. No one archetype is representative of a discrete land cover type except perhaps where the land surface is barren or for very dense forests such as are found in the tropics. The highest variability, but also perhaps the highest information content is potentially

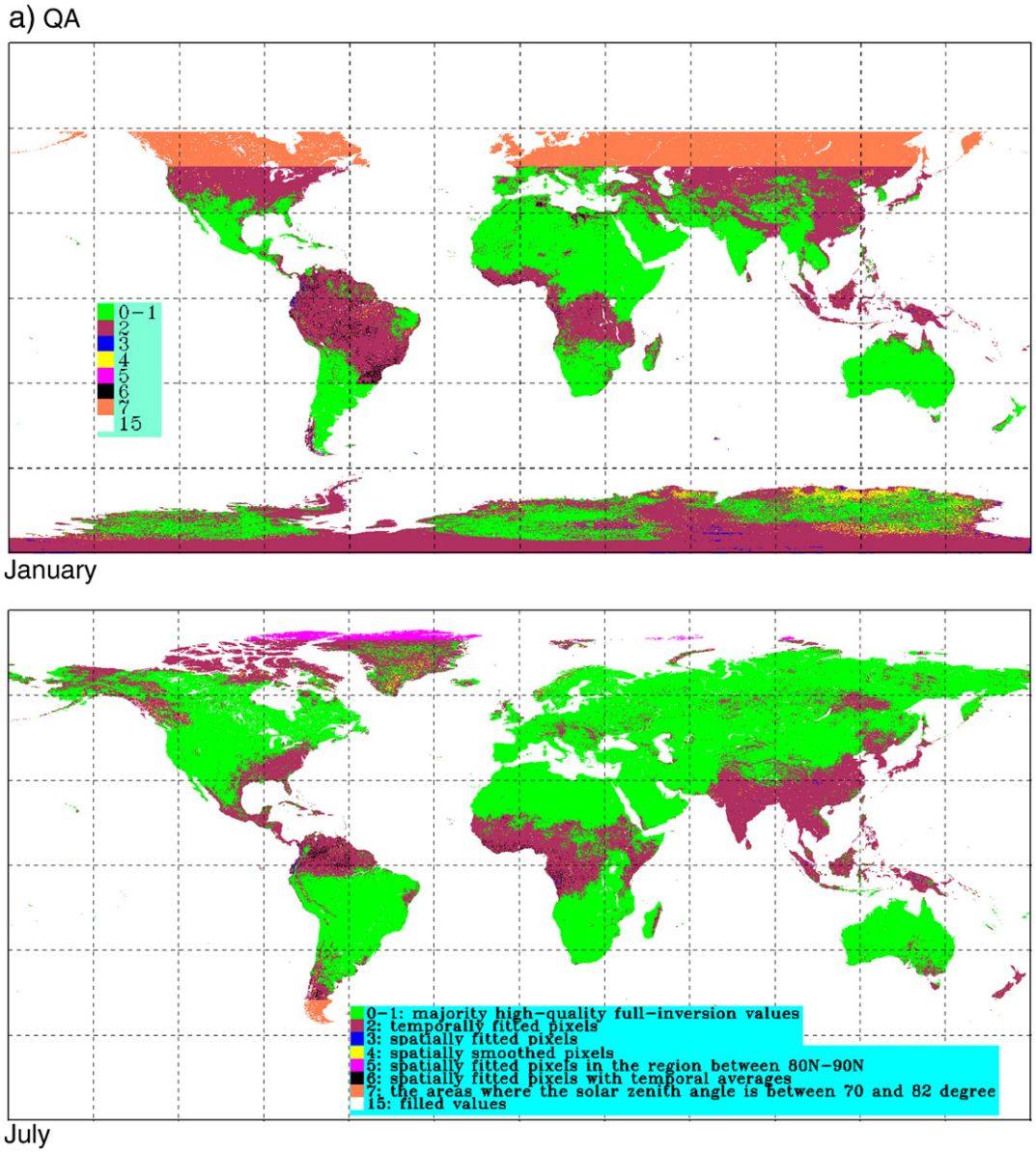

Fig. 12. Global patterns for AFX archetypes for the four most functionally sensitive spectral bands for DOY 001 and 185 and corresponding quality assurance (QA). a) Global pattern of QA for data for DOY 001 and 185; b) Red band AFX for DOY 001 and 185; c) NIR band AFX for DOY 001 and 185.

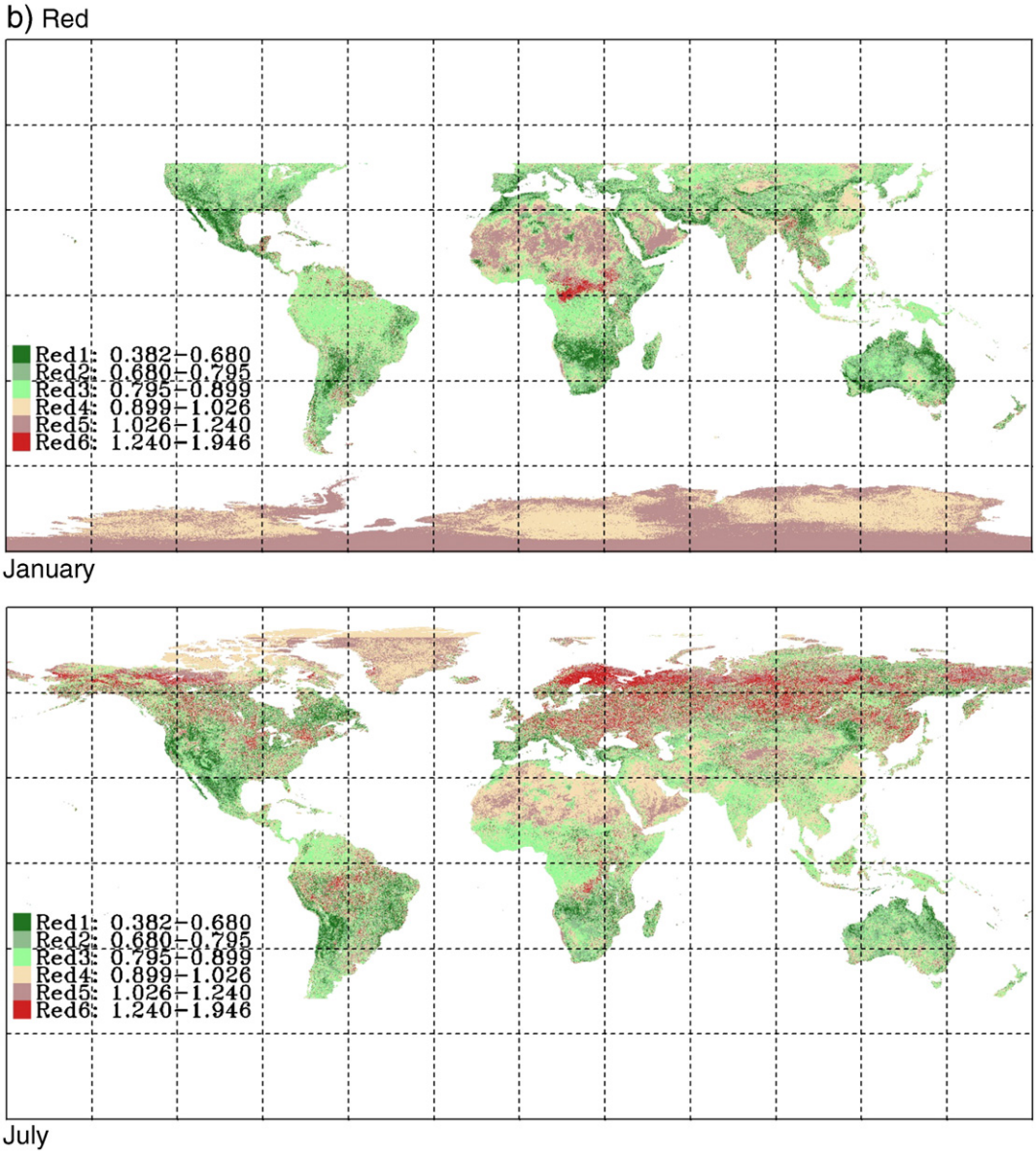

Fig. 12 (*continued*).

found in the land covers with heterogeneous arrangements and densities of multi-layer objects and leaf-canopies. Consequently, at fine scale, e.g., a savanna with dense grassy understory may be less distinct from a woodland, than would be a degraded savanna with predominantly bare soil underlying the tree canopy. Further analysis of data at regional and landscape scales, appropriate to aggregation of the archetype differences, is needed to complement and enhance the general patterns and associations with land cover types.

Some detailed aspects and assumptions associated with the derivation of AFX and the BRDF typology require further examination and discussion. First, the assumption that a given heterogeneous land surface reflectance can be viewed as *a combination of material surface scattering and volume scattering* may need further examination for land covers such as ice and snow that can also exhibit significant forward scattering characteristic. Second, the derivation of AFX does depend upon the fit of the model. The kernel-driven linear BRDF model was originally designed to comprise a collection of different kernels for various land cover types. These kernel functions are derived from different assumptions for vegetation canopy structure (e.g., small or large LAI for RossThin or RossThick kernels for continuous vegetation canopy; sparse or dense tree density for LiSparse and LiDense kernels for discrete crown), and view and illumination geometries (e.g., reciprocity; non-reciprocity). Difficulties in implementing these multi-kernel models without imposing severe a priori assumptions and in assigning consistent quality evaluations have caused a move away from multiple models during operational MODIS BRDF retrieval. However, use of a single uniform model may result in some discrepancies in modeling the radiation field (Hu et al., 1997; Wanner et al., 1995), especially in hotspot direction (Huang, Jiao, Dong, Zhang, & Li, 2012; Maignan et al., 2004). Further testing with alternative kernels is a continual process although to date, the RTLSR model continues to represent the largest number of surface types (Huang et al., 2012). Finally, it must be pointed out yet again that the kernel functions of kernel-driven BRDF model are not necessarily orthogonal (Lucht et al., 2000) and the model anisotropic parameters (f_{geo} and f_{vol}) do not necessarily rise and fall in a totally complementary fashion. This results in a few, rare situations where the geometric-optical and volumetric parameters are both increasing and/or decreasing. These few extreme anisotropic parameters

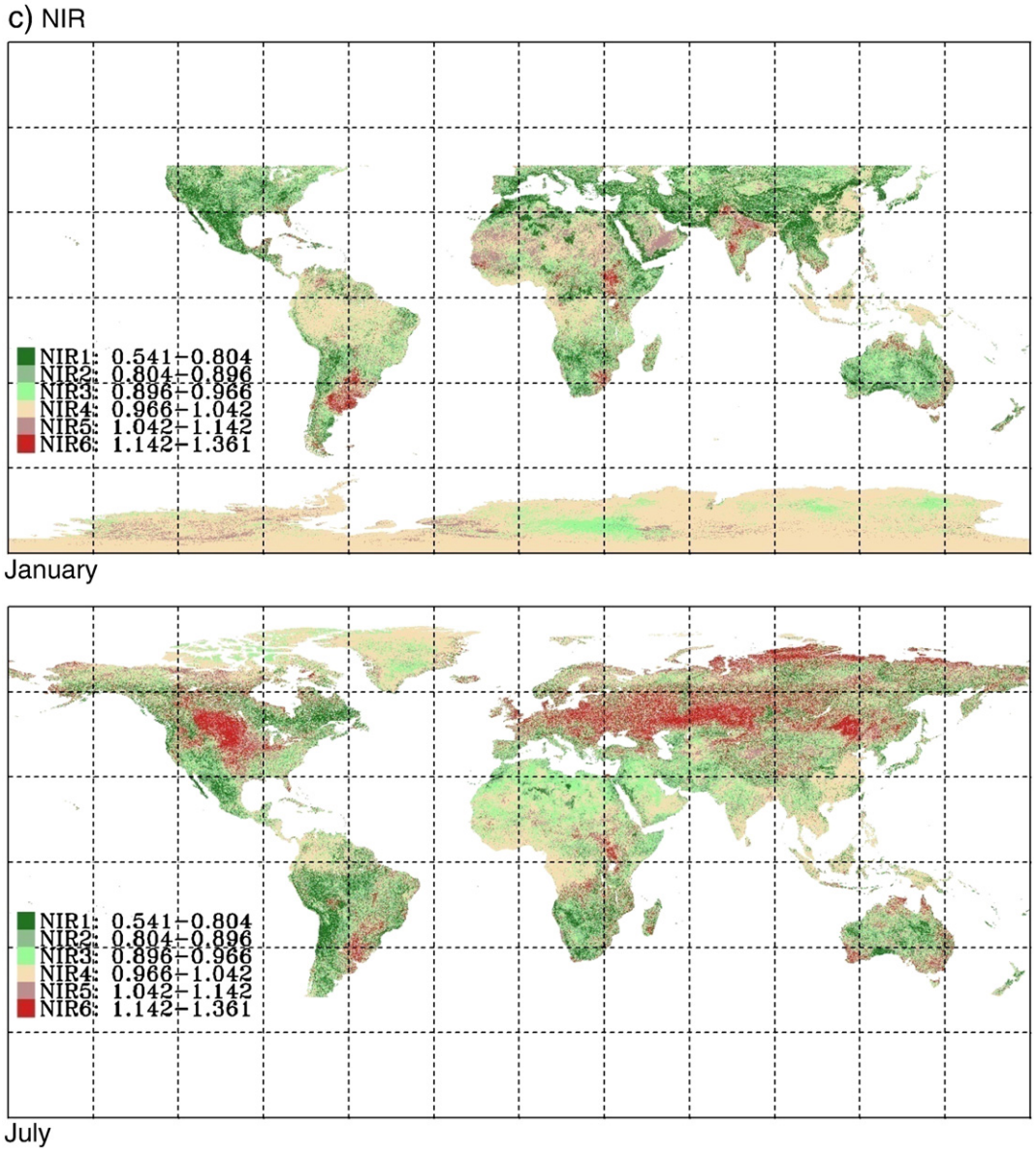

Fig. 12 (*continued*).

could generate a few BRDF shapes that enlarge the within-class variances of BRDF archetypal classes and therefore need to be further examined in near future.

5. Conclusions

In this study, the AFX summarizes BRDF archetypes and presents the uniqueness of this information beyond NDVI (e.g., somewhat orthogonal to NDVI for MODIS data) as it reflects a non-linear response to changes in surface structural properties from major scattering from discrete objects through the use of model simulation. The AFX supports a BRDF-based classification scheme for BRDF typology. The BRDF archetype classes derived by this method and ecological biomes being explored need not coincide. Additionally, these BRDF archetypes could be used as a priori knowledge in estimation of biophysical parameters for certain ecological applications (e.g., surface albedo in a separate paper). These results demonstrates that the AFX shows promise as an additional source of information from anisotropic reflectance patterns in relation to different vegetation properties beyond that which can be obtained from spectral information alone. These vegetation properties are strongly associated with anisotropic reflectance, and shadowing, and different scale variations in clumping, gap fractions and sunlit and shaded leaf fractions, and thus need to be further explored in near future. Many physical models (e.g., Li–Strahler model, 1992; Strahler–Jupp model, 1990; 5-Scale model, 1997, etc.) have shown that the vegetation canopy architectures strongly determines the canopy BRDF (please see the review by Strahler, 1997). Recent research has shown that addition of BRDF shape information can improve overall classification accuracy by ~5% beyond spectral Nadir-BRDF Adjusted Reflectances (NBAR) for POLDER and MODIS data at the region-to-global scale (DE Colstoun & Walthall, 2006; Jiao & Li, 2012; Jiao et al., 2011). However, an archetype-based BRDF characterization of the terrestrial surface may also provide meaningful structural classes in modeling domains, and advance the role of BRDF shapes in applications beyond mere assistance with classification.

Acknowledgments

This work was supported by the NSFC (41171261 and 40871193) and the National Basic Research Program (973 Program, 2013CB733400).

Thanks are due to Feng Gao (USDA/USA) and Jicheng Liu (NOAA/USA) for his helpful suggestions and Jing M. Chen (University of Toronto, Canada) for kindly providing the 5-Scale BRDF model for simulations. The comments and recommendations by the anonymous reviewers are also greatly appreciated.

References

Archibald, S., & Scholes, R. J. (2007). Leaf green-up in a semi-arid African savanna—Separating tree and grass responses to environmental cues. *Journal of Vegetation Science*, *18*, 583–594.

Asner, G. P. (2000). Contributions of multi-view angle remote sensing to land-surface and biogeochemical research. *Remote Sensing Reviews*, *18*, 137–162.

Bartrlev, S. A., Belward, A. S., Erchov, D.V., & Lsaev, A. S. (2003). A new SPOT4-VEGETATION derived land cover map of Northern Eurasia. *International Journal of Remote Sensing*, *24*, 1977–1982.

Bicheron, P., Defourney, P., Brockmann, C., Schouten, L., Vancutsem, C., Huc, M., et al. (2008). *GLOBCOVER*. Products description and validation report. Toulouse, FranceMedias France/POSTEL (47 pp.).

Bicheron, P., & Leroy, M. (2000). Bidirectional reflectance distribution function signatures of major biomes observed from space. *Journal of Geophysical Research*, *105*, 26669–26681.

Boegh, E., Soegaard, H., Broge, N., Hasager, C. B., Jensen, N. O., Schelde, K., et al. (2002). Airborne multispectral data for quantifying leaf area index, nitrogen concentration, and photosynthetic efficiency in agriculture. *Remote Sensing of Environment*, *81*, 179–193.

Bréon, F. -M., & Vermote, E. (2012). Correction of MODIS surface refl ectance time series for BRDF effects. *Remote Sensing of Environment*, *125*, 1–9.

Ceccato, P., Tarantola, S., Jacquemoud, S., Gregoire, J. M., & Flasse, S. (2001). Detecting vegetation leaf water content using reflectance in the optical domain. *Remote Sensing of Environment*, *77*, 22–23.

Chen, J. M., & Cihlar, J. (1996). Retrieving leaf area index of boreal conifer forests using Landsat TM images. *Remote Sensing of Environment*, *55*, 153–162.

Chen, J. M., & Leblanc, S. G. (1997). A four-scale bidirectional reflectance model based on canopy architecture. *IEEE Transactions on Geoscience and Remote Sensing*, *35*, 1316–1337.

Chen, J. M., & Leblanc, S. G. (2001). Multiple-scattering scheme useful for geometric optical modeling. *IEEE Transactions on Geoscience and Remote Sensing*, *39*, 1061–1071.

Chen, J. M., Liu, J., Leblanc, S. G., Lacaze, R., & Roujean, J. L. (2003). Multi-angular optical remote sensing for assessing vegetation structure and carbon absorption. *Remote Sensing of Environment*, *84*, 516–525.

Chen, J. M., Menges, C. H., & Leblanc, S. G. (2005). Global mapping of foliage clumping index using multi-angular satellite data. *Remote Sensing of Environment*, *97*, 447–457.

Chopping, M., Moisen, G. G., Su, L. H., Laliberte, A., Rango, A., Martonchik, J. V., et al. (2008). Large area mapping of southwestern forest crown cover, canopy height, and biomass using the NASA Multiangle Imaging Spectro-Radiometer. *Remote Sensing of Environment*, *112*, 2051–2063.

Cohen, W. B., Maiersperger, T. K., Gower, S. T., & Turner, D. P. (2003). An improved strategy for regression of biophysical variables and Landsat ETM + data. *Remote Sensing of Environment*, *84*, 561–571.

DE Colstoun, B. E. C., & Walthall, C. L. (2006). Improving global scale land cover classifications with multi-directional POLDER data and a decision tree classifier. *Remote Sensing of Environment*, *100*, 474–485.

Deering, D. W., Eck, T. F., & Banerjee, B. (1999). Characterization of the reflectance anisotropy of three boreal forest canopies in spring–summer. *Remote Sensing of Environment*, *67*, 205–229.

Deering, D. W., Middleton, E. M., & Eck, T. F. (1994). Reflectance anisotropy for a spruce-hemlock forest canopy. *Remote Sensing of Environment*, *47*, 242–260.

Deering, D. W., Middleton, E. M., Irons, J. R., Blad, B.L., Waltershea, E. A., Hays, C. J., et al. (1992). Prairie grassland bidirectional reflectance measured by different instruments at the FIFE site. *Journal of Geophysical Research-Atmospheres*, *97*, 18887–18903.

Defries, S., & Townshend, J. R. G. (1994). NDVI-derived land cover classifications at global scale. *International Journal of Remote Sensing*, *15*(17), 3567–3586.

D'Entremont, R. P., Schaaf, C. B., Lucht, W., & Strahler, A. H. (1999). Retrieval of red spectral albedo and bidirectional reflectance using AVHRR HRPT and GOES satellite observations of the New England region. *Journal of Geophysical Research-Atmospheres*, *104*, 6229–6239.

Di Bella, C. M., Paruelo, J. M., Becerra, J. E., Bacour, C., & Baret, F. (2004). Effect of senescent leaves on NDVI-based estimates of fAPAR: Experimental and modelling evidences. *International Journal of Remote Sensing*, *25*, 5415–5427.

Friedl, M.A., McIver, D. K., Hodges, J. C. F., Zhang, X. Y., Muchoney, D., Strahler, A. H., et al. (2002). Global land cover mapping from MODIS: Algorithms and early results. *Remote Sensing of Environment*, *83*, 168–182.

Friedl, M.A., Sulla-Menashe, D., Tan, B., Schneider, A., Ramankutty, N., Sibley, A., et al. (2010). MODIS collection 5 global land cover: Algorithm refinements and characterization of new datasets. *Remote Sensing of Environment*, *114*, 168–182.

Galvao, L. S., Roberts, D. A., Formaggio, A.R., Numata, I., & Breunig, F. M. (2009). View angle effects on the discrimination of soybean varieties and on the relationships between vegetation indices and yield using off-nadir Hyperion data. *Remote Sensing of Environment*, *113*, 846–856.

Gao, F., Li, X., Strahler, A., & Schaaf, C. (2000). Evaluation of the Li transit kernel for BRDF modeling. *Remote Sensing Reviews*, *19*, 205–224.

Gao, F., Schaaf, C. B., Strahler, A. H., Jin, Y., & Li, X. (2003). Detecting vegetation structure using a kernel-based BRDF model. *Remote Sensing of Environment*, *86*, 198–205.

Haboudane, D., Miller, J. R., Pattey, E., Zarco-Tejada, P. J., & Strachan, I. (2004). Hyperspectral vegetation indices and novel algorithms for predicting green LAI of crop canopies: Modeling and validation in the context of precision agriculture. *Remote Sensing of Environment*, *90*, 337–352.

Hansen, M. C., Defries, R. S., & Townshend, J. R. G. (2000). Global land cover classification at 1 km spatial resolution using a classification tree approach. *International Journal of Remote Sensing*, *21*(6&7), 1331–1364.

Hansen, M. C., DeFries, R. S., Townshend, J. R. G., Carroll, M., Dimiceli, C., & Sohlberg, R. A. (2003). Global percent tree cover at a spatial resolution of 500 meters: First results of the MODIS vegetation continuous fields algorithm. *Earth Interactions*, *7*, 1–15.

Hansen, M. C., DeFries, R. S., Townshend, J. R. G., Sohlberg, R., Dimiceli, C., & Carroll, M. (2002). Towards an operational MODIS continuous field of percent tree cover algorithm: Examples using AVHRR and MODIS data. *Remote Sensing of Environment*, *83*, 303–319.

Harada, C., Sumi, A., & Ohmori, H. (2003). Seasonal and year-to-year variations of rainfall in the Sahara desert region based on TRMM PR data. *Geophysical Research Letters*, *30*(6), 1288–1291.

Hasegawa, K., Matsuyama, H., Tsuzuki, H., & Sweda, T. (2010). Improving the estimation of leaf area index by using remotely sensed NDVI with BRDF signatures. *Remote Sensing of Environment*, *114*, 514–519.

He, L., Chen, J. M., Pisek, J., Schaaf, C. B., & Strahler, A. H. (2012). Global clumping index map derived from the MODIS BRDF product. *Remote Sensing of Environment*, *119*, 118–130.

Heiskanen, J., & Kivinen, S. (2008). Assessment of multispectral, -temporal and -angular MODIS data for tree cover mapping in the tundra–taiga transition zone. *Remote Sensing of Environment*, *112*, 2367–2380.

Hill, M. J., Averill, C., Jiao, Z., Schaaf, C. B., & Armston, J.D. (2008). Relationship of MISR RPV parameters and MODIS BRDF shape indicators to surface vegetation patterns in an Australian tropical savanna. *Canadian Journal of Remote Sensing*, *34*, S247–S267.

Hill, M. J., Roman, M.O., Schaaf, C. B., Hutley, L., Brannstrom, C., Etter, A., et al. (2011). Characterizing vegetation cover in global savannas with an annual foliage clumping index derived from the MODIS BRDF product. *Remote Sensing of Environment*, *115*, 2008–2024.

Holben, B. N. (1986). Characteristics of maximum-value composite images from temporal AVHRR data. *International Journal of Remote Sensing*, *7*, 1417–1434.

Hu, B. X., Lucht, W., Li, X. W., & Strahler, A. H. (1997). Validation of kernel-drives semiempirical models for the surface bidirectional reflectance distribution function of land surfaces. *Remote Sensing of Environment*, *62*, 201–214.

Huang, X., Jiao, Z., Dong, Y., Zhang, H., & Li, X. (2012). Analysis of BRDF and albedo retrieved by kernel-driven models using field measurements. *IEEE Journal of Selected Topics in Applied Earth Observations and Remote Sensing*, 1–13.

Huete, A. (1988). A soil adjusted vegetation index (SAVI). *Remote Sensing of Environment*, *25*, 295–309.

Irons, J. R., Campbell, G. S., Norman, J. M., Graham, D. W., & Kovalick, W. M. (1992). Prediction and measurement of soil bidirectional reflectance. *IEEE Transactions on Geoscience and Remote Sensing*, *30*, 249–260.

Jiao, Z., & Li, X. (2012). Effects of multiple view angles on the classification of forward-modeled MODIS reflectance. *Canadian Journal of Remote Sensing*, *38*(4), 461–474.

Jiao, Z., Woodcock, C., Schaaf, C. B., Tan, B., Liu, J., Gao, F., et al. (2011). Improving MODIS land cover classification by combining MODIS spectral and angular signatures in a Canadian boreal forest. *Canadian Journal of Remote Sensing*, *37*(2), 184–203.

Jin, Y., Schaaf, C. B., Gao, F., Li, X., Strahler, A. H., Lucht, W., et al. (2003). Consistency of MODIS surface bidirectional reflectance distribution function and albedo retrievals: 1. Algorithm performance. *Journal of Geophysical Research-Atmospheres*, *108*, 4158.

Kimes, D. S. (1983). Dynamics of directional reflectance factor distributions for vegetation canopies. *Applied Optics*, *22*, 1364–1372.

Kimes, D. S., Newcomb, W. W., Nelson, R. F., & Schutt, J. B. (1986). Directional reflectance distributions of a hardwood and pine forest canopy. *IEEE Transactions on Geoscience and Remote Sensing*, *GE-24*, 281–293.

Kimes, D. S., Newcomb, W. W., Tucker, C. J., Zonneveldt, I. S., Van Wijngaarden, W., De Leeuw, J., et al. (1985). Direction reflectance factor distributions for cover types of Northern Africa. *Remote Sensing of Environment*, *18*, 1–19.

Lacaze, R., Chen, J. M., Roujean, J. L., & Leblanc, S. G. (2002). Retrieval of vegetation clumping index using hot spot signatures measured by POLDER instrument. *Remote Sensing of Environment*, *79*, 84–95.

Leblanc, S. G., & Chen, J. M. (2001). A practical scheme for correcting multiple scattering effects on optical LAI measurements. *Agricultural and Forest Meteorology*, *110*, 125–139.

Leblanc, S. G., Chen, J. M., White, H. P., Latifovic, R., Lacaze, R., & Roujean, J. -L. (2005). Canada-wide foliage clumping index mapping from multiangular POLDER measurements. *Canadian Journal of Remote Sensing*, *31*, 364–376.

Leroy, M., & Bréon, F. M. (1996). Angular signatures of surface reflectances from airborne POLDER data. *Remote Sensing of Environment*, *57*, 97–107.

Leroy, M., & Roujean, J. L. (1994). Sun and view angle corrections on reflectances derived from NOAA/AVHRR data. *IEEE Transactions on Geoscience and Remote Sensing*, *32*, 684–697.

Li, X. W., Gao, F., Chen, L. Z., & Strahler, A. (1999). Derivation and validation of a new kernel for kernel-driven BRDF models. *Remote Sensing for Earth Science, Ocean, and Sea Ice Applications*, *3868*, 368–379.

Li, X., & Strahler, A. H. (1992). Geometric-optical bidirectional reflectance modeling of the discrete crown vegetation canopy: Effect of crown shape and mutual shadowing. *IEEE Transactions on Geoscience and Remote Sensing*, *30*, 276–292.

Li, X. W., Strahler, A. H., & Woodcock, C. E. (1995). A hybrid geometric optical-radiative transfer approach for modeling albedo and directional reflectance of discontinuous canopies. *IEEE Transactions on Geoscience and Remote Sensing*, *33*, 466–480.

Loveland, T. R., Brown, J. F., Ohlen, D. O., Zhu, Z., Yang, L., Merchant, J. W., et al. (2000). Development of a global land cover characteristics database and IGBP DISCover from 1 km AVHRR data. *International Journal of Remote Sensing, 21*, 1303–1330.

Lucht, W., & Lewis, P. (2000). Theoretical noise sensitivity of BRDF and albedo retrieval from the EOS-MODIS and MISR sensors with respect to angular sampling. *International Journal of Remote Sensing, 21*, 81–98.

Lucht, W., Schaaf, C. B., & Strahler, A. H. (2000). An algorithm for the retrieval of albedo from space using semiempirical BRDF models. *IEEE Transactions on Geoscience and Remote Sensing, 38*, 977–998.

Maignan, F., Breon, F. M., & Lacaze, R. (2004). Bidirectional reflectance of earth targets: Evaluation of analytical models using a large set of spaceborne measurements with emphasis on the hot spot. *Remote Sensing of Environment, 90*, 210–220.

Martonchik, J. V., Pinty, B., & Verstraete, M. M. (2002). Note on "An improved model of surface BRDF-atmospheric coupled radiation". *IEEE Transactions on Geoscience and Remote Sensing, 40*, 1637–1639.

Myneni, R. B., Hall, F. G., Sellers, P. J., & Marshak, A. L. (1995). The interpretation of spectral vegetation indexes. *IEEE Transactions on Geoscience and Remote Sensing, 33*, 481–486.

Myneni, R. B., Ramakrishna, R., Nemani, R., & Running, S. W. (1997). Estimation of global leaf area index and absorbed par using radiative transfer models. *IEEE Transactions on Geoscience and Remote Sensing, 35*, 1380–1393.

Nolin, A. W. (2004). Towards retrieval of forest cover density over snow from the Multi-angle Imaging Spectro Radiometer (MISR). *Hydrological Processes, 18*, 3623–3636.

Ranson, K. J., Biehl, L. L., & Bauer, M. E. (1985). Variation in spectral response of soybeans with respect to illumination, view and canopy geometry. *International Journal of Remote Sensing, 6*, 1827–1842.

Roman, M.O., Gatebe, C. K., Schaaf, C. B., Poudyal, R., Wang, Z., & King, M.D. (2011). Variability in surface BRDF at different spatial scales (30 m–500 m) over a mixed agricultural landscape as retrieved from airborne and satellite spectral measurements. *Remote Sensing of Environment, 115*, 2184–2203.

Román, M. O., Gatebe, C. K., Shuai, Y., Wang, Z., Gao, F., Masek, J., He, T., et al. (2013). Use of in-situ and airborne multiangle data to assess MODIS- and Landsat-based estimates of directional reflectance and albedo. *IEEE Transactions on Geoscience and Remote Sensing, 51*(3), 1393–1404.

Ross, J. K. (1981). *The radiation regime and architecture of plant stands*. Norwell, MA Dr. W. Junk (392 pp.).

Roujean, J. L., & Lacaze, R. (2002). Global mapping of vegetation parameters from POLDER multiangular measurements for studies of surface–atmosphere interactions: A pragmatic method and its validation. *Journal of Geophysical Research-Atmospheres, 107*.

Roujean, J. -L., Leroy, M., & Deschamps, P. -Y. (1992). A bidirectional reflectance model of the earth's surface for the correction of remote sensing data. *Journal of Geophysical Research, 97*, 20455–20468.

Ryu, Y. R., Sonnentag, O., Nilson, T., Vargas, R., Kobayashi, H., Wenk, R., et al. (2010). How to quantify tree leaf area index in an open savanna ecosystem a multi-instrument and multi-model approach. *Agricultural and Forest Meteorology, 150*, 63–76.

Sandmeier, S., & Deering, D. W. (1999). Structure analysis and classification of boreal forests using airborne hyperspectral BRDF data from ASAS. *Remote Sensing of Environment, 69*, 281–295.

Sandmeier, S., Muller, C., Hosgood, B., & Andreoli, G. (1998). Physical mechanisms in hyperspectral BRDF data of grass and watercress. *Remote Sensing of Environment, 66*, 222–233.

Schaaf, C. B., Gao, F., Strahler, A. H., Lucht, W., Li, X., Tsang, T., et al. (2002). First operational BRDF, albedo nadir reflectance products from MODIS. *Remote Sensing of Environment, 83*, 135–148.

Schaaf, C. B., Liu, J., Gao, F., & Strahler, A. H. (2011). MODIS albedo and reflectance anisotropy products from Aqua and Terra. In B. Ramachandran, C. Justice, & M. Abrams (Eds.), *Land remote sensing and global environmental change: NASA's Earth Observing System and the Science of ASTER and MODIS. Remote Sensing and Digital Image Processing Series, 11*, Springer-Verlag (873 pp.).

Shuai, Y., Masek, J. G., Gao, F., & Schaaf, C. B. (2011). An algorithm for the retrieval of 30-m snow-free albedo from Landsat surface reflectance and MODIS BRDF. *Remote Sensing of Environment, 115*, 2204–2216.

Shuai, Y., Schaaf, C. B., Strahler, A. H., Liu, J., & Jiao, Z. (2008). Quality assessment of BRDF/albedo retrievals in MODIS operational system. *Geophysical Research Letters, 35*.

Strahler, A. H. (1997). Vegetation canopy reflectance modeling-recent developments and remote sensing perspectives. *Remote Sensing Reviews, 15*, 179–194.

Strahler, A. H., & Jupp, D. L. B. (1990). Modeling bidirectional reflectance of forests and woodlands using Boolean models and geometric optics. *Remote Sensing of Environment, 34*, 153–166.

Strugnell, N. C., & Lucht, W. (2001). An algorithm to infer continental-scale albedo from AVHRR data, land cover class, and field observations of typical BRDFs. *Journal of Climate, 14*, 1360–1376.

Strugnell, N., Lucht, W., & Schaaf, C. (2001). A global albedo data set derived from AVHRR data for use in climate simulations. *Geophysical Research Letters, 28*, 191–194.

Su, L., Chopping, M. J., Rango, A., Martonchik, J. V., & Peters, D. P. C. (2007). Support vector machines for recognition of semi-arid vegetation types using MISR multi-angle imagery. *Remote Sensing of Environment, 107*, 299–311.

Tsay, S.C., King, M.D., Arnold, G. T., & Li, J. Y. (1998). Airborne spectral measurements of surface anisotropy during SCAR-B. *Journal of Geophysical Research-Atmospheres, 103*, 31943–31953.

Tucker, C. J. (1980). Remote sensing of leaf water content in the near infrared. *Remote Sensing of Environment, 10*, 23–32.

Vermote, E., Justice, C. O., & Breon, F. M. (2009). Towards a generalized approach for correction of the BRDF effect in MODIS directional reflectances. *IEEE Transactions on Geoscience and Remote Sensing, 47*, 898–908.

Vierling, L. A., Deering, D. W., & Eck, T. F. (1997). Differences in arctic tundra vegetation type and phenology as seen using bidirectional radiometry in the early growing season. *Remote Sensing of Environment, 60*, 71–82.

Wang, Z., Schaaf, C. B., Lewis, P., Knyazikhin, Y., Schull, M.A., Strahler, A. H., et al. (2011). Retrieval of canopy height using moderate-resolution imaging spectroradiometer (MODIS) data. *Remote Sensing of Environment, 115*, 1595–1601.

Wanner, W., Li, X., & Strahler, A. H. (1995). On the derivation of kernels for kernel-driven models of bidirectional reflectance. *Journal of Geophysical Research, 100*, 21077–21089.

Zhang, X., Friedl, M.A., Schaaf, C. B., Strahler, A. H., Hodges, J. C. F., Gao, F., et al. (2003). Monitoring vegetation phenology using MODIS. *Remote Sensing of Environment, 84*, 471–475.